COMPRESSIBLE FLOWS FOR FLUIDIC CONTROL IN MICRODEVICES

by

Dustin S. Chang

A dissertation submitted in partial fulfillment
of the requirements for the degree of
Doctor of Philosophy
(Chemical Engineering)
in The University of Michigan
2010

Doctoral Committee:

Professor Mark A. Burns, Chair
Professor Robert M. Ziff
Associate Professor Luis P. Bernal
Associate Professor Michael Mayer

© Dustin S. Chang

2010

To my mom and dad,

Sweson and Chaohui,

and my grandparents,

Po-High and Peyuk …

Thank you for all your sacrifices.

ACKNOWLEDGEMENTS

To the casual observer, a doctoral thesis may appear to be the product of a single dedicated—albeit misguided—individual after multiple years of toil. Anyone that has survived the experience will most assuredly tell you that he could not have done it without the many people who supported him along the way.

Beginning long before graduate school, my family has been a constant source of encouragement, well-meaning criticism, and material support. I am hugely grateful for my aunts and uncles who never failed to go the extra mile in taking care of me, teaching me, and challenging me to improve. Aunt Hsueh-Rong, Aunt Nancy, Aunt Chao-Lin, Uncle Jeff, Aunt Tina, and Uncle Ming ... Thank you for your love. The only people potentially deserving greater appreciation than these are my mother and father and my grandparents. I have no doubt that none of my meager accomplishments would have been possible without your prayers and unconditional support, both moral and financial. I also have no doubt that all of the aforementioned people are infinitely more enamored with the idea of a Ph.D. in the family than I am.

On an occasion such as this, it is impossible not to speak of the individuals who set me down this path. More than one of them would likely be surprised to learn the extent of their influence given that, in many cases, I myself did not realize they were influencing me. From the time I was little, Uncle Jeff infected me with his desire to learn

everything about everything. Although my intellectual curiosity has not developed to be near as boundless, Uncle Jeff's imprint on me is evident. Since we became friends in elementary school, Neerav always pushed me to exceed expectations (even if often for no better reason than juvenile competitiveness) and still today possesses the uncanny ability to conjure up the perfect thought experiment to reason through any situation. In high school, Fred Buono captured my interests with his lucid explanation of cell biology and generous stream of encouragement. I did not end up a biologist, but the interests Mr. Buono inspired are unmistakable. At Stanford, I was taught by Jen-Tsan Chi and Gerry Fuller. Jen-Tsan provided me my first research experience in the Brown Lab; I imagine he was nonplussed by my ambivalence at the time because I failed to realize how formative an experience it would be. I can recall listening to Professor Fuller describe his research about surface tension and rheological effects, which would induce me to mentally roll my eyes and wonder how anyone could be enthusiastic about something so seemingly insignificant. I now direct you to examine the subject of this thesis and relish the irony.

During my time in Ann Arbor, I have met many excellent people who blessed me with their friendship. Katie, Lisa, David, Ted, and Barb welcomed me to Ann Arbor and went to extraordinary lengths to make me feel at home. I sincerely appreciate the effort by the folks from Knox and the Law School to involve me in their gatherings and intramural teams. In particular, I have to thank Jeremiah and Mary Jo for their unfailing hospitality and the many delicious meals that came out of their kitchen. I also thank Razi for being a constant source of assistance and levity in the cleanroom, in the lab, and in the garage.

Finally, I must acknowledge the people in Chemical Engineering. Dylan, K.C., Kyung, and Brian, some of whom have since moved on, patiently mentored me when I first arrived and knew nothing. I can only hope that I have set as good an example as they set for me. Sean and Ramsey, and later Eric, brought a collaborative element that had been sorely lacking in the Burns Group. In particular, I have enjoyed working with Sean, whose originality fortuitously complemented my own lack of creativity and whose willingness to spend time helping me reason through counterintuitive observations assuaged my research frustrations more than just once. With Jihyang, Irene, Jae Sung, Dana, and Colin, the group is in good hands. Thankfully, I do not foresee a reversion to the old group dynamic. My advisor, Mark Burns, has demonstrated the impressive ability to guide his students' development without grabbing the wheel. Although our shared penchant for procrastination was in all likelihood nonideal, what needed to get done somehow always got done. He is unquestionably the best doctoral advisor I have ever had. My sincere thanks go to Professor Ziff, Professor Bernal, and Professor Mayer for donating so much time and effort over the past few years to provide invaluable feedback and advice regarding my dissertation. I also thank Connie, Claire, Leslie, Jane, and Shelley for all their help with the everyday tasks that only seem trivial when they are done correctly.

TABLE OF CONTENTS

DEDICATION ii

ACKNOWLEDGEMENTS iii

LIST OF FIGURES viii

LIST OF TABLES xi

CHAPTER

1. INTRODUCTION 1

Motivation 1

Overview of developments in microscale flow control 3

Organization of this dissertation 7

References 9

2. AN ELECTRONIC VENTURI-BASED PRESSURE MICROREGULATOR ... 10

Introduction 10

Materials and Methods 12

Fluidic channel microfabrication 12

Electronic component microfabrication 14

Device assembly 14

Device operation 15

Results and Discussion 16

Concept 16

Electronically-controlled pressure regulation 20

Droplet movement using Venturi pressure microregulator..................25

Conclusions 30

References 32

3. A VENTURI MICROREGULATOR ARRAY MODULE FOR DISTRIBUTED PRESSURE CONTROL 33

Introduction 33

Materials and Methods 37

Venturi microregulator array fabrication 37
Open fluidic network fabrication 39
Device operation 40

Results and Discussion 41

Geometric design and tuning 41
Multiple microregulator operation 46
Fluid manipulation in open microchannel networks 49

Conclusions 55

References 57

4. VISCOUS EFFECTS IN LOW RE PLANAR MICRONOZZLES 58

Introduction 58

Materials and Methods 61

Micronozzle design and fabrication 61
Micronozzle operation and characterization 64
Micronozzle simulation 65

Results and Discussion 66

Reynolds number dependence of micronozzle behavior 66
Viscous wall effects 70
Other gases 80

Conclusions 85

References 87

5. CONCLUSIONS AND FUTURE WORK 88

Conclusions 88

Continuing work 90

References 95

LIST OF FIGURES

Figure 1.1 Examples of integrated microfluidic devices. ………………………………... 2

Figure 1.2 Schematic of electroosmotic flow. ………………………………………… 3

Figure 1.3 Schematic of electrowetting. ………………………………………………. 4

Figure 1.4 Schematic of capacitive mechanical displacement micropump. …………... 5

Figure 1.5 Schematic of pneumatic membrane displacement microvalves. …………... 6

Figure 2.1 Process flow diagram for microfabrication of channel layer (a-f) and electronics layer (g-i) of Venturi microregulator. …………………………13

Figure 2.2 Schematic of Venturi pressure microregulator. ……………………………17

Figure 2.3 Variation of constriction pressure ($P_{\text{constrict}}$) with inlet pressure (P_{in}) at different channel depths. ………………………………………………..18

Figure 2.4 Variation of constriction pressure with increasing inlet pressure for different nozzle scalings in the *xy*-plane at a uniform depth of 80 µm. ……………. 19

Figure 2.5 Variation of constriction pressure with increasing inlet pressure for an 80 µm deep Venturi nozzle at 30°C and 95°C. ……………………………….20

Figure 2.6 Linear variation of constriction pressure with increasing temperature at constant inlet pressures of 115 kPa (93 µm-deep nozzle) and 110 kPa (80 µm-deep nozzle). ……………………………………………………… 21

Figure 2.7 Analytical approximation of the axial evolution of the *z*-dimensional temperature gradient. ………………………………………………... 23

Figure 2.8 Linear variation of constriction pressure with increasing temperature remains consistent over multiple inlet pressures. ………………………… 24

Figure 2.9 Venturi pressure microregulator with constant width (550 µm) serpentine channel attached to sidearm for demonstrating controlled droplet motion. ……………………………………………………… 25

Figure 2.10 Venturi temperature (measured by RTD1 in Fig. 2.9) and droplet velocity plotted over time for one switching cycle. 26
Figure 2.11 Schematic illustrating droplet movement in an open channel system. 28
Figure 3.1 Multiple Venturi microregulator module. 36
Figure 3.2 Fabrication process flow. 38
Figure 3.3 Alternate microregulator array geometries. 43
Figure 3.4 Plot of constriction pressure behavior with varying inlet pressure at room temperature before (open symbols) and after (filled symbols) geometric tuning, which allows constriction pressure matching at the desired inlet pressure. 44
Figure 3.5 Graph of variation among the constriction pressures of arrayed microregulators in different device types. 45
Figure 3.6 Variation of constriction pressure with microregulator temperature in a geometrically tuned device at P_{in} = 200 kPa. 47
Figure 3.7 Effect of thermal and pressure crosstalk. 48
Figure 3.8 Schematic of fluidic network controlled by microregulator array. 50
Figure 3.9 Images of various droplet manipulations carried out in fluidic network pictured in Fig. 3.8. 52
Figure 3.10 Moving one droplet while keeping a second droplet stationary. 54
Figure 3.11 Three-layer device integrating Venturi microregulator array and microfluidic network. 56
Figure 4.1 Experimental micronozzle structure. 62
Figure 4.2 Flow characteristics of experimental micronozzles. 69
Figure 4.3 Simulated throat velocity distributions. 71
Figure 4.4 Simulated boundary layer development with Re_{throat}. 73
Figure 4.5 Deviation of experimental micronozzle performance from isentropic flow. 75
Figure 4.6 Simulated mass flow in micronozzles with varying area ratio and heat addition. 76
Figure 4.7 Simulated boundary layer thickness with heat addition for H = 80 μm. 77

Figure 4.8 Simulated velocity and density profiles with heat addition for H = 80 μm. 78
Figure 4.9 Changes in mass flow with heat addition in experimental micronozzles. ... 79
Figure 4.10 .Experimental variation of throat pressure with inlet pressure for helium operated micronozzles. 81
Figure 4.11 Mass flux in experimental micronozzles operated with helium (*top*) and Argon (*bottom*). 82
Figure 4.12 Changes in throat pressure and mass flow with heat addition in experimental helium and argon micronozzles. 84
Figure 5.1 Schematic of a surface dielectric barrier discharge plasma actuator. 90
Figure 5.2 Plasma actuators mounted on an airfoil being used to control boundary layer separation. 91
Figure 5.3 Voltage-current characteristics of low-density plasma discharge regimes. 92
Figure 5.4 Candidate electrode geometry for microplasma actuator. 94

LIST OF TABLES

Table 4.1 Area ratios of fabricated micronozzles ……………………….................... 62

Table 4.2 Gas Properties at 20 °C, 1 atm ……………………………………….….... 80

CHAPTER 1

INTRODUCTION

Motivation

The advancement of microfluidics has led to tremendous growth in chemical and biomedical applications, including microreactors, biochemical assays, and physical sensing and measurement.[1,2,3] This growth is mostly attributable to three advantages associated with decreasing length scale: increased efficiency, higher throughput, and greater portability. Microfluidic systems provide efficiency gains over their macroscale counterparts both via reduced sample and reagent consumption, as well as decreased time scales of operation. The higher packing density of fluidic structures resulting from a decreased length scale permits throughput enhancement, facilitating the simultaneous processing of multiple samples or multiple assays using a single sample. Improvements in portability are particularly desirable for point-of-care biomedical diagnostics. However, one major reason for the slow development of commercial, point-of-care platforms is the failure of flow control system miniaturization to keep pace with the scaling of the microfluidic devices they support.

Generally, integrated microfluidic devices follow one of two design paradigms as shown in Fig. 1.1—a sample is transported to the reagents and the various functional regions of the device, or a sample is introduced at the functional region and reagents are

transported to the sample. In either case, successful operation requires an appropriate control mechanism for flow handling. Early successes have fueled the desire for increasing automation, complexity, and portability of microfluidic devices. The critical role of flow control to device operation guarantees that satisfaction of this demand will hinge on the continued development of more versatile, yet reliable, integrated microfluidic flow control systems.

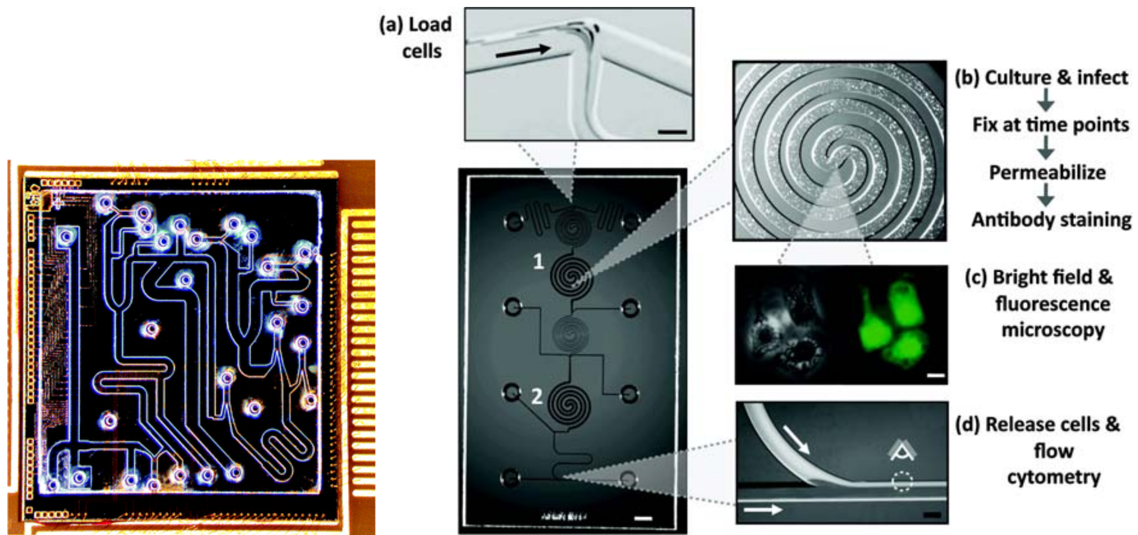

Figure 1.1. Examples of integrated microfluidic devices. (*Left*) Device for identifying strains of influenza developed by Pal, *et al*. A DNA sample is transported to the various functional areas of the device where different unit operations are performed. This assay format is most common for nucleic acid analyses. (Figure taken from R. Pal and M Yang, *et al*. *Lab Chip* 2005.) (*Right*) Device for cell signaling studies developed by Srivastava, *et al*. Cells are introduced and sequestered in the spiral culture chambers. Additional reagents are transported to this central location for interaction with the cells. This format is commonly used for cell studies and immunoassays. (Figure taken from N. Srivastava, *et al*. *Anal Chem* 2009.)

Overview of developments in microscale flow control

Microscale flow control systems cover an extensive range of actuation mechanisms, each of which presents its own advantages and limitations. These mechanisms can be separated into two primary categories: electrokinetic and pressure-driven. Electrokinetic methods use electric fields to exert force on fluids and particles.[4] Of these methods, electroosmotic flow (EOF) has been the most popular on account of its speed, robustness, and ease of implementation, requiring only bare glass channels, electrodes, and an appropriate voltage source. A liquid electrolyte in contact with a solid dielectric spontaneously forms a diffuse charge layer along their interface. If an electric field is imposed over the liquid, the charge layer is dragged along with the interior fluid toward the electrode of opposite polarity, resulting in EOF (Fig. 1.2). Electroosmostic flow is well-suited for biological assays due to the near exclusive use of aqueous samples and reagents; however, this mechanism is clearly ineffective for gases or nonpolar liquids.

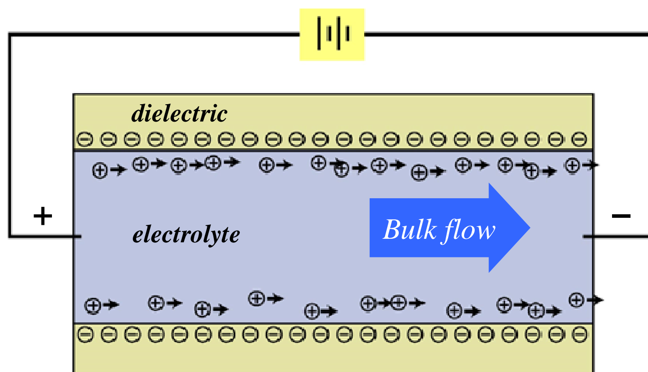

Figure 1.2. Schematic of electroosmotic flow. A diffuse charge layer is formed in the liquid electrolyte upon contact with the solid dielectic. Under the influence of an electric field, the charge layer moves toward the electrode of opposite polarity, dragging the bulk fluid as well.

Pressure-driven flows encompass a much broader variety of actuation mechanisms, all of which act by creating a pressure differential across a volume of fluid. One example relying on surface tension is capillary-driven flow. Passively actuated devices using this mechanism tend to be robust, portable, and simple to operate, but these

advantages come at the expense of operational versatility due to fixed flow paths and designed dependence on specific liquid properties. Capillary-driven flow can also be actively controlled as in the case of electrowetting (Fig. 1.3), where tiled electrodes are selectively activated to modify the contact angle between liquid and substrate, generating a pressure gradient in the liquid.

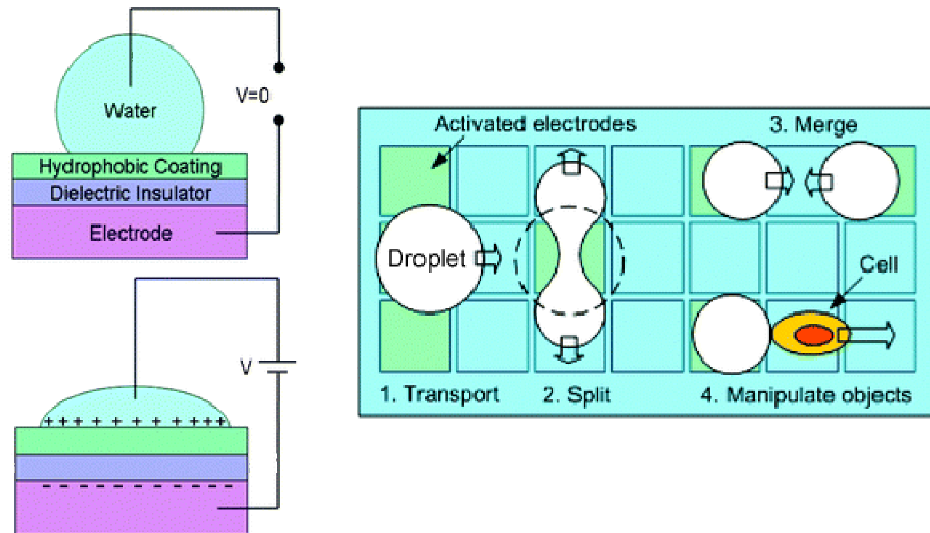

Figure 1.3. Schematic of electrowetting. The contact angle between the liquid droplet and solid substrate is decreased upon application of an electric field. Tiled electrodes activated according to their relative positions can be used to transport, split, and merge droplets. (Figure taken from Y. Zhao, *et al*. *Lab Chip* 2007.)

The most common method of generating pressure-driven flow is mechanical displacement. Unlike capillary-driven flow, this method generally functions independently of the properties of the substrate and the fluid being acted upon. Mechanical displacement micropumps can be actuated using electrostatics, thermal expansion, piezoelectrics, electromagnetics, or any of a multitude of other mechanisms. These pumps most often consist of a reciprocating diaphragm paired with a flow rectification scheme as shown in Fig. 1.4.

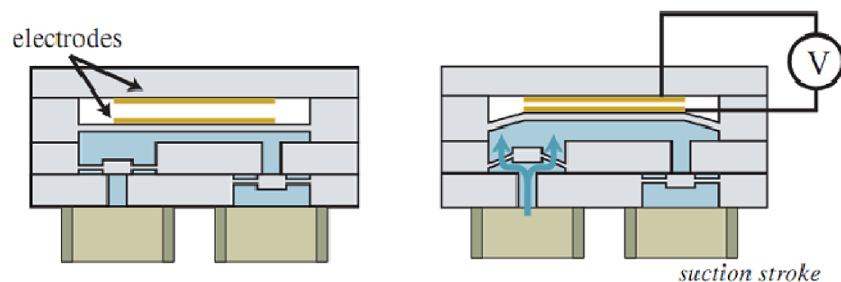

Figure 1.4. Schematic of capacitive mechanical displacement micropump. The reciprocating diaphragm is actuated by the electrostatic interaction of the electrodes. Flow is rectified by a pair of check valves. (Figure taken from D.J. Laser, *et al*. *J Micromech Microeng* 2004.)

Application of pressure from external sources is perhaps the most straightforward method for generating pressure-driven flow. The simplest example of such a source is a syringe pump. Alternatively, pneumatics may also be used to apply either direct or indirect pressure. Direct pressure methods use temporal or mechanical attenuation of macroscale pneumatic sources to apply controllable pressures for precise displacement of microscale fluid volumes. One popular method of indirect pneumatic flow control is the membrane deflection valve (Fig. 1.5). Here, a pneumatic control channel and the controlled fluidic channel are separated by a flexible membrane. The membrane deflects into the fluidic channel, pinching it off, when the control channel is pressurized. This structure can function as a standalone valve, or a serial arrangement of three such structures can function as a peristaltic pump. Other pressure-driven flow control methods include centrifugal actuation, where the device is rotated at a specific sequence of angular velocities to drive liquid motion, and more recently introduced acoustic mechanisms, such as surface acoustic waves and acoustic streaming.

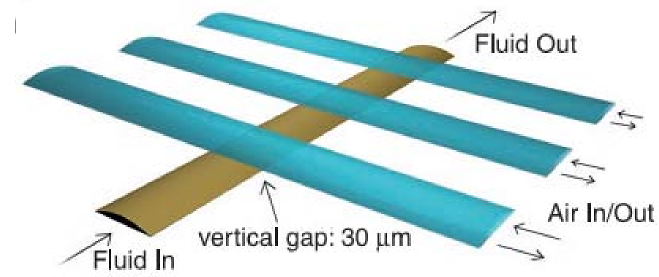

Figure 1.5. Schematic of pneumatic membrane displacement microvalves. The membranes separating the air channels and the fluid channel at their points of overlap are deflect downward upon pressurization of the air channels, pinching off the fluid channel. (Figure taken from M.A. Unger, *et al*. *Science* 2000.)

Organization of this dissertation

This dissertation centers on the behavior of gas flow in microfluidic devices and its utilization for flow control. In Chapter 2, we introduce a new method for pressure-driven microscale fluidic control using a gas flow. We describe an electronically controlled, Venturi-based pressure microregulator that can output pressures both greater and less than atmospheric pressure over a range of 2 kPa from a single pressurized air input. The microregulator operates by using embedded resistive heaters to vary the temperature of a choked gas flow through a converging-diverging nozzle between 25°C and 85°C with a control resolution of 33 Pa $°C^{-1}$. We established the switching speed of the microregulator by accurately moving droplets in microchannels via pneumatic propulsion. Droplet deceleration from approximately 1 cm s^{-1} to zero velocity required less than 0.8 s. Also of great practical importance, the component is readily integrable into most device designs containing fluidic channels and electronics without introducing additional fabrication complexity.

One advantage of the pressure microregulator presented in Chapter 2 is the potential for integrating multiple independently controlled instances of the component that share the same input into one device. Given that pressure-driven flow control is critical to the operation of many microfluidic devices, comparmentalization of this functionality into a standalone module possessing a simple interface would allow a welcome reduction in the number of separate connections to off-chip pneumatic sources required for fluidic control. Ideally, such a module would also be sufficiently compact for implementation in portable platforms. In Chapter 3, we show the feasibility of using a modular array of Venturi pressure microregulators for coordinated droplet manipulation.

The arrayed microregulators share a single pressure input and are capable of outputting electronically controlled pressures that can be independently set between -1.3 kPa and +1.3 kPa. Using the array, we demonstrate loading, splitting, merging, and independent movement of multiple droplets in a valveless microchannel network.

Chapter 4 investigates the physical phenomena enabling the operational mechanism of the Venturi microregulator in greater detail. The lack of understanding concerning gas flows at the length scales ($\sim 10^{-5}$ m) and flow regimes ($Re \sim 10^{3}$) most common to microfluidics forces the design of such components to be largely by trial and error. We combine experimental measurement and simulation tools to characterize the interplay between the key dimensions of the nozzle geometry and the fundamental length scale of viscous wall effects. Additionally, we use the integrated temperature control capability of the Venturi microregulator to observe the effects of heat addition on mass flow in a choked, low *Re* system. Because the flow is choked, compressibility effects are important, particularly under non-adiabatic conditions. Comparison of the flow behavior of helium and argon to our experiments with air aids in this analysis. Our study aims to provide improved qualitative understanding of boundary layer dynamics in bounded gas phase microflows. The low dynamic viscosity of gases allows access to a larger range of flow regimes through judicious selection of the geometric length scale than is possible with liquids at the microscale. Ultimately, comprehension of the interactions among these flow phenomena will be necessary for their utilization in functional design.

Resources

---

[1] Erickson D, Li D (2004) Integrated microfluidic devices. Anal Chim Acta 507:11-26. doi: 10.1016/j.aca.2003.09.019

[2] Ohno K, Tachikawa K, Manz A (2008) Microfluidics: Applications for analytical purposes in chemistry and biochemistry. Electrophoresis 29:4443-4453.

[3] Jensen KF (2001) Microreaction engineering – is small better? Chem Eng Sci 56: 293-303.

[4] Wong PK, Wang TH, Deval JH, Ho CM (2004) Electrokinetics in micro devices for biotechnology applications. IEEE/ASME Transactions on Mechtronics 9:366-376.

[5] Pal R, Yang M, Lin R, Johnson BN, Srivastava N, Razzacki SZ, Chomistek KJ, Heldsinger DC, Haque RM, Ugaz VM, Thwar PK, Chen Z, Alfano K, Yim MB, Krishnan M, Fuller AO, Larson RG, Burke DT, Burns MA (2005) An integrated microfluidic device for influenza and other genetic analyses. Lab Chip 5:1024-1032. doi: 10.1039/b505994a

[6] Srivastava N, Brennan JS, Renzi RF, Wu M, Branda SS, Singh AK, Herr AE (2009) Fully integrated microfluidic platform enabling automated phosphoprofiling of macrophage response. Anal Chem 81:3261-3269. doi: 10.1021/ac8024224

[7] Zhao Y, Cho SK (2007) Micro air bubble manipulation by electrowetting on dielectric (EWOD): transporting, splitting, merging and eliminating of bubbles. Lab Chip 7:273-280. doi: 10.1039/b616845k

[8] Laser DJ, Santiago JG (2004) A review of micropumps. J Micromech Microeng 14:R35-R64. doi: 10.1088/0960-1317/14/6/R01

[9] Unger MA, Chou HP, Thorsen T, Scherer A, Quake SR (2000) Monolithic microfabricated valves and pumps by multilayer soft lithography. Science 288:113-116.

CHAPTER 2

AN ELECTRONIC VENTURI-BASED PRESSURE MICROREGULATOR

Introduction

Many microfluidic devices rely on pneumatic control to function. Microfabricated devices for chemical synthesis[1,2,3] and analysis[4,5] may manipulate one or more gas-phase reagents and constitute a subset of devices that employ pneumatics expressly to move gases. A larger group of microfluidic devices uses pneumatics to move and mix liquids. For example, integrated devices for biological analysis move liquid samples between dedicated areas for performing specific functions, such as reagent metering, mixing, thermocycling, and analyte detection.[6] A number of these devices handle liquid samples as multi-phase flows, the simplest being an air and liquid droplet-based system in which gas flow propels the liquid samples. Irrespective of form, material, or function, accurate fluidic control remains vital to essentially all microfluidic chip designs, in which both flow rate[7,8] and sample positioning[9,10] can be critical to successful operation.

The most straightforward method for droplet movement is direct application of externally controlled pressure sources. Syringe pumps provide an ideal mechanism for liquid continuous flow systems,[11] but for pneumatically driven droplets, regulating the minute pressure differences needed for precise liquid motion using these arrangements is unrealistic. Eddings, *et al.* circumvented this problem using a gas permeation pump.[12]

Pressurized air or vacuum applied to a control reservoir separated from the liquid channels by a thin, gas-permeable polydimethylsiloxane (PDMS) membrane attenuated the input pressures to achieve manageable flow rates. Serial deflection of pneumatically controlled PDMS membranes has been widely used as displacement pumps for pulsatile fluidic movement.[13,14] Alternatively, Pal, *et al.* utilized temporal attenuation for fluidic control in an integrated analysis device by applying pulsed air pressure to incrementally move a droplet.[9] On-chip methods for pressure generation include thermopneumatic pumping for displacing droplets over small distances[15] and thermal transpiration.[16]

The on-chip fluidic control scheme we have devised employs Venturi pressure regulators for generating gas flow and is ideally suited for pneumatically controlled droplet movement. A Venturi produces a relative vacuum without moving parts and consists of a converging-diverging channel with a sidearm. Chung, *et al.* fabricated a bidirectional microfluidic manipulation system consisting of an unbranched channel with a converging-diverging Venturi nozzle at each end.[17] Setting the pressure gradient between the Venturis determined the velocity of a liquid plug loaded into the channel. Independent control of the air flow rate through each Venturi allowed arbitrary reversal of the liquid motion by modifying the pressure gradient down the length of the sealed channel.

We have used the Venturi concept to design and characterize an on-chip pressure microregulator capable of accurately controlling pressures with a resolution of 33 Pa $°C^{-1}$ over a range of approximately 2 kPa. The design includes no moving parts, simplifying fabrication and minimizing the potential of mechanical failure. This microregulator is readily integrable into microdevices containing microchannels and electronic components

without increasing fabrication complexity. Unlike any existing pressure regulator to our knowledge, this device can output positive and negative pressures relative to atmospheric pressure from a single pressurized air input. The pressure output is electronically controlled, which potentially allows multiple instances to be individually addressable while sharing a common air input. Thus, in addition to being used alone, this component can be implemented in conjunction with existing pneumatic microfluidic control schemes to minimize the external infrastructure and the number of off-chip connections required to operate a given device.

Materials and Methods

Fluidic channel microfabrication

The microfabricated devices consist of two pieces of bonded glass with fluidic channels etched in the upper piece and electronic components patterned on the lower piece. Chromium and gold (500/3500 Å) were evaporated on Borofloat glass wafers (700 μm thick, 10 cm diameter) cleaned in piranha solution (H_2SO_4/H_2O_2, 3:1). Photoresist (Microposit SC 1827; Shipley Co., Marlborough, MA) was spun on at 2000 rpm and soft baked on a hot plate at 100°C for 2.5 min. The fluidic channel pattern was exposed and then developed in MF319 (Shipley Co.) for 1 min. The developed wafer was hard baked at 140°C for 45 min. The gold was etched for 2 min (gold etchant TFA; Transene Co., Danvers, MA), and the chromium was etched for 2 min (chromium etchant CR-14; Cynatek Corp., Fremont, CA), masking the glass wafer with the metal channel pattern. The exposed glass was etched in hydrofluoric acid (49% HF, CMOS grade; J.T. Baker,

Philipsburg, NJ) to obtain channel depths of 24 μm, 48 μm, 72 μm, 76 μm, 80 μm, 93 μm, and 151 μm. The channel cross-section after etching was approximately trapezoidal with the length of the shorter base equal to the width of the masked feature and the length of the longer base equal to the length of the shorter base plus a lateral etch equal to the downward etch on each side. The wafer was diced to separate the individual devices. Air inlet holes were drilled using a high-speed drill press with a diamond-tipped bit (1.5 mm diameter; UKAM Industrial Superhard Tools, Valencia, CA). Smaller liquid inlet holes of 0.5 mm diameter were drilled by electrochemical discharge machining.[18]

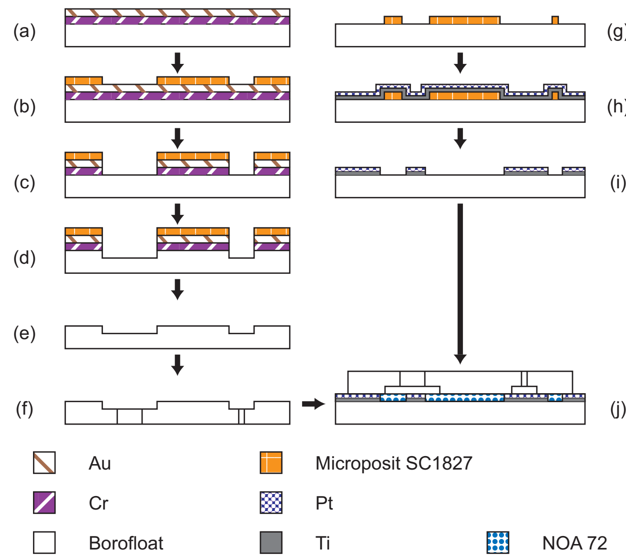

Figure 2.1: Process flow diagram for microfabrication of channel layer (*a-f*) and electronics layer (*g-i*) of Venturi microregulator. (*a*) Bare Borofloat wafer is coated with 500 Å Cr/2500 Å Au by e-beam evaporation. (*b*) Photoresist is spin-coated onto the metal-covered wafer and patterned with the channel geometry. (*c*) Exposed areas of the metal masking layer are etched away. (*d*) Exposed areas of the Borofloat wafer are etched in HF to the desired depth. (*e*) Photoresist and metal mask are stripped. (*f*) Fluidic access holes are drilled. (*g*) Photoresist is spin-coated onto a second bare Borofloat wafer and patterned with the heater and RTD layout. (*h*) Patterned wafer is coated with 300 Å Ti/1000 Å Pt by e-beam evaporation. (*i*) Excess metal is removed by dissolving photoresist in sonicated acetone bath. (*j*) Devices are aligned and assembled using UV curable adhesive.

Electronic component microfabrication

The heaters and four-point resistive temperature detectors (RTD) were patterned in a single metal layer using a liftoff process. Bare Borofloat wafers cleaned in piranha solution were lithographically processed as in the channel fabrication procedure to generate a photoresist pattern outlining the desired metal lines but were not hard baked. Titanium and platinum (300/1000 Å) were evaporated onto the developed wafer. The wafer was sonicated in acetone (CMOS grade; J.T. Baker) for 10 min to liftoff unwanted metal. The measured resistances of the heaters and RTDs were approximately 40 Ω and between 500 and 2000 Ω, respectively. The wafer was diced to obtain the individual devices.

Device assembly

The diced devices were cleaned with acetone, isopropyl alcohol, and de-ionized water. After visual alignment of the two device layers, UV curable optical glue (NOA 72; Norland Products, Cranbury, NJ) was applied at the edge of the device and allowed to wick in between the layers by capillary action. The glue was cured according to the manufacturer's instructions. The positioning of electronic components in the design prevents liquid contact during device operation, alleviating the need for an electrical isolation layer. Each glued device was affixed using standard quick cure epoxy and wire bonded to a printed circuit board. Syringe tips (Part Number 5114-B-90; EFD Inc., East Providence, RI) glued to glass capillaries (2 mm I.D.) were attached to the fluid inlets with epoxy (Steel Weld Epoxy; ITW Performance Polymers, Riviera Beach, FL) for interfacing with off-chip connections.

Device operation

Lab air supply, controlled by a pressure regulator (Model Number 3476A; Matheson Gas Products Inc, Irving, TX), was continuously fed to the gas inlet of the device. The heaters and RTDs on the device were controlled by a DC power supply (Model Number HY5003; Mastech, Hong Kong), two data acquisition (DAQ) boards (PCI-6031E and PCI-6704; National Instruments, Austin, TX), two connector blocks (SCB-100 and SCB-68; National Instruments), a custom signal conditioning circuit, a computer, and a LabVIEW program (National Instruments). To calibrate the thermal sensors, the entire device was incubated in a convection oven whose temperature was ramped from room temperature to 100°C. Concurrently, a current of 3 mA was sent through two leads of the four-point RTDs while the voltage across the other two leads was recorded in a LabVIEW program. Once converted to resistance, a linear fit of the resistance and temperature data was generated. A proportional-integral (PI) control algorithm used in conjunction with this linear fit regulated the voltage across the microfabricated heaters. All pressure measurements were taken using an electronic pressure sensor (Strain Gage Panel Meter DP25B-S; Omega, Stamford, CT). Droplet velocity was calculated by measuring the displacement of the liquid menisci in video of device operation (29.97 fps) recorded using a camera (CCD-300 monochrome video camera; Dage-MTI, Michigan City, IN) connected to a stereo microscope (SZH10; Olympus America Inc., Center Valley, PA) at 7x magnification.

Results and Discussion

Concept

The core component of our microregulator, shown in Fig. 2.2, is a Venturi. Air moving at subsonic velocities through the constricted channel must accelerate as the channel narrows and decelerate as the channel widens to maintain a constant volumetric flow rate. For energy to be conserved, a corresponding decrease/increase in fluid pressure must accompany increases/decreases in the fluid velocity, assuming negligible viscous energy loss. If the pressure change is sufficiently large, a vacuum relative to atmospheric pressure is produced at the constriction, drawing fluid into the sidearm. This Venturi effect is a special case of Bernoulli's principle given by

$$P_{in} + \rho_{in} \frac{u_{in}^2}{2} = P_{constrict} + \rho_{constrict} \frac{u_{constrict}^2}{2} + \Delta P_{viscous} \tag{2.1}$$

in which P is pressure, ρ is density, and u is velocity at the inlet and constriction, respectively. The term $\Delta P_{\text{viscous}}$ represents the pressure drop attributable to viscous energy dissipation between the inlet and the constriction.

The pressure at the constriction of a Venturi is primarily determined by the inlet pressure. Figure 2.3a shows the pressure at the constriction ($P_{\text{constrict}}$) of the Venturi defined in Fig. 2.2a for inlet pressures (P_{in}) ranging from 60 kPa to 170 kPa at room temperature. This pressure range was selected because it covers the transition to choked flow, is relatively low, and is generally available in standard laboratory facilities. Raising the inlet pressure with the outlet held at atmospheric pressure accelerates the subsonic gas flow, increases the pressure difference between the constriction and outlet, and consequently produces increasingly stronger vacuum. When the flow at the constriction

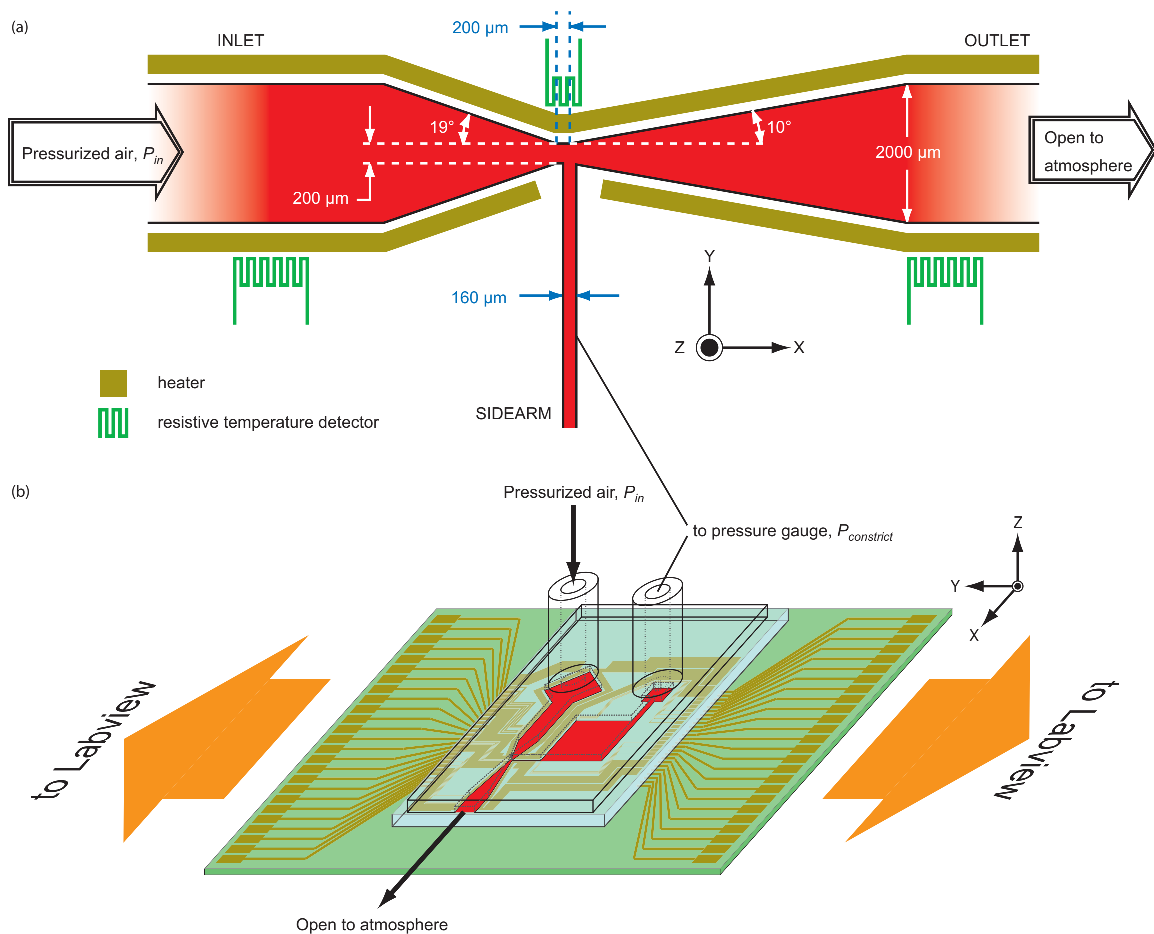

Figure 2.2. Schematic of Venturi pressure microregulator. (*a*) Venturi nozzle geometry with resistive temperature detector (RTD) and heater layout. The outlet is open to the atmosphere while the sidearm can connect to any arbitrary channel geometry. The pressure at the throat of the converging-diverging nozzle determines whether a positive or negative pressure gradient exists down the sidearm. The channel depth in the *z*-direction is uniform across the entire geometry. (*b*) Experimental setup for measuring $P_{\mathrm{constrict}}$. The experimental setup for droplet movement is identical except for the coupling to the pressure gauge, which is absent.

becomes sonic, the flow chokes[19] and further increase of the inlet pressure does not increase the fluid velocity. Instead, higher inlet pressures raise the constriction pressure.

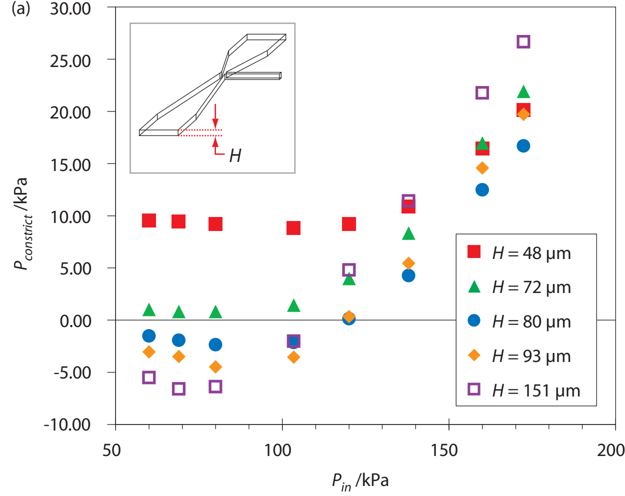

Figure 2.3. Variation of constriction pressure ($P_{\text{constrict}}$) with inlet pressure (P_{in}) at different channel depths. Experimental measurement of $P_{\text{constrict}}$ at different values of P_{in}. Deeper nozzles generate larger pressure differences between the inlet and constriction. The standard deviation about each data point is approximately 0.45 kPa.

At certain inlet pressures, Fig. 2.3a indicates that the constriction pressure can be positive or negative depending on the Venturi geometry. In addition to the inlet pressure, the constriction pressure in a Venturi also depends on the relative contribution of viscous forces to the pressure drop in the flow ($\Delta P_{\text{viscous}}$). For our calculations, we have used a Poiseuille flow treatment of an incompressible Newtonian fluid such that

$$\Delta P_{viscous} = Q \cdot R_h = Q \cdot \frac{128\mu L}{\pi D_h^4} \tag{2.2}$$

where Q is the volumetric flow rate, μ is the dynamic viscosity, L is the channel length, and D_{h} is the hydraulic diameter. A hydraulic diameter for channels that do not have a circular cross-section can be calculated as

$$D_h = \frac{4A}{P} \tag{2.3}$$

where A is the cross-sectional area and P is the wetted perimeter. Although particular formulations for the viscous pressure drop may differ slightly, $\Delta P_{\text{viscous}}$ varies inversely with D_h^2 in each case. Therefore, as hydraulic diameter shrinks to microscale dimensions, the Reynolds number (Re) decreases and viscous forces rapidly increase relative to inertial forces, eventually violating the initial assumption of negligible viscous energy loss. The increased thickness of the viscous sublayer—the region of the flow near the channel walls in which viscous forces dominate—relative to the hydraulic diameter decreases the difference in velocity and subsequently the difference in pressure between the inlet and constriction. For our geometry, depths less than approximately 72 μm failed to create a negative constriction pressure at any inlet pressure. Shrinking the hydraulic diameter by proportionally reducing the lateral dimensions of the nozzle also disrupts the Venturi effect as the constriction width approaches a similar critical dimension, as shown in Fig. 2.4.

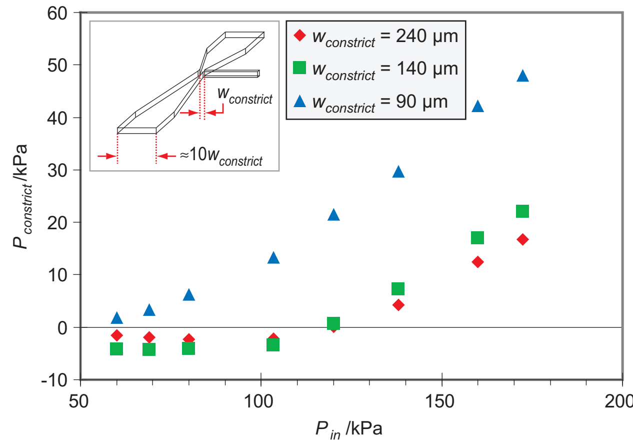

Figure 2.4. Variation of constriction pressure with increasing inlet pressure for different nozzle scalings in the xy-plane at a uniform depth of 80 μm. The width of the Venturi throat for each device is indicated. All other linear dimensions of the geometry in Fig. 2.2a are scaled proportionally. The standard deviation about each data point is approximately 0.37 kPa.

Electronically controlled pressure regulation

By tuning our Venturi geometry such that channel depth is comparable to viscous boundary layer thickness, we can regulate the constriction pressure at a fixed inlet pressure by controlling the Venturi temperature, as shown in Fig. 2.5. A channel depth of

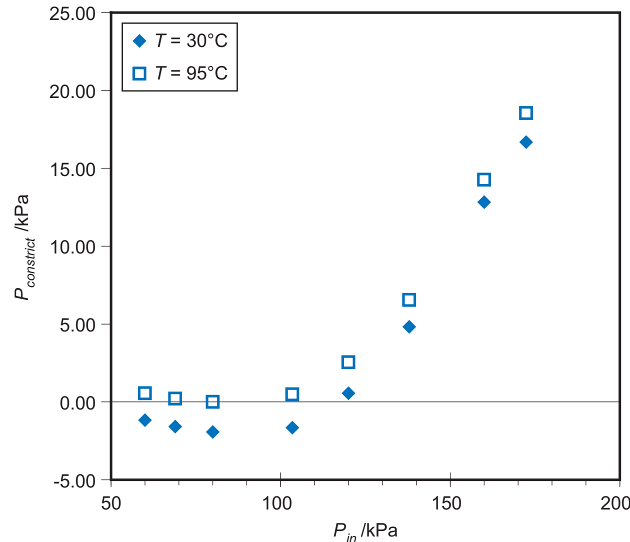

Figure 2.5. Variation of constriction pressure with increasing inlet pressure for an 80 µm deep Venturi nozzle at 30°C and 95°C. Elevated temperature corresponds to increased constriction pressure for all inlet pressures. To facilitate positive/negative switching, we selected an optimal inlet operating pressure of 110 kPa. At this inlet pressure, the associated 30°C and 95°C curves symmetrically bracket a neutral constriction pressure with a difference of 2.1 kPa. Each data point represents one measurement.

80 µm was selected because this geometry exhibited the weakest dependence of $P_{\text{constrict}}$ on P_{in} out of all devices capable of generating negative pressures. All observed constriction pressures at 95°C exceed their corresponding measurements at 30°C. Because the viscosity of gases increases with temperature, increasing the Venturi temperature thickens the viscous sublayer and alters the magnitude of viscous forces relative to inertial forces in the flow, causing the constriction pressure to increase.

Greater air viscosity therefore corresponds to a shallower channel depth; in each case, *Re* decreases and viscous sublayer thickness increases relative to the hydraulic diameter.

Thermal control enables precise regulation of pressure output because the dependence of constriction pressure on temperature is linear. Figure 2.6 shows a pressure variation of 33 Pa °C^{-1} at an inlet pressure of 110 kPa, providing a control range of 2.1 kPa, for a channel depth of 80 μm. We selected an operating inlet pressure of 110 kPa because at this inlet pressure, the 30°C and 95°C curves in Fig. 2.5 symmetrically bracket a neutral constriction pressure such that the middle of the operating temperature range corresponds to neutral constriction pressure. For a depth of 93 μm, we observed a weaker temperature dependence of 27 Pa °C^{-1} at an inlet pressure of 115 kPa. In general, smaller hydraulic diameters yield superior range and reproducibility of pressure control while larger hydraulic diameters produce finer control resolution. This result is due to the decreasing change in relative viscous sublayer thickness with increasing hydraulic diameter for any given temperature change.

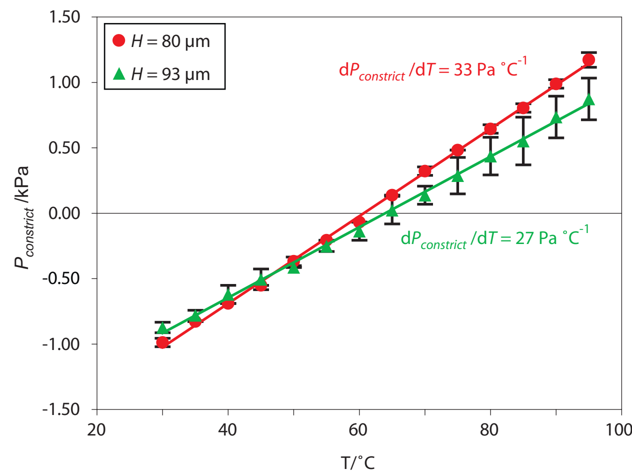

Figure 2.6. Linear variation of constriction pressure with increasing temperature at constant inlet pressures of 115 kPa (93 μm-deep nozzle) and 110 kPa (80 μm-deep nozzle). Error bars indicate one standard deviation above and below the mean of no fewer than three experiments.

The larger error bars of the 93 μm device in Fig. 2.6 indicate that stable temperature control is more difficult in deeper channels, producing greater variation in constriction pressure, particularly at higher temperatures. One reason for this is the higher air velocity in the 93 μm device due to a higher operating inlet pressure and lower fluidic resistance, leading to greater convective heat transfer than in the 80 μm device. Figure 2.7 illustrates this trend using a worst-case analytical approximation of the axial evolution of the z-dimensional temperature distribution in the channel, assuming a uniform flow velocity. At a distance of one (nondimensionalized by the entrance length) away from the inlet, the temperature variation transverse to the flow direction has fallen to ten percent of the total difference between the initial fluid temperature and the heater temperature. This entrance length varies inversely with the square of channel height and linearly with flow velocity, such that deeper channels require longer distances to heat the fluid to the desired temperature. Using this model, the calculated entrance length corresponding to our 80 μm device is 4 mm, while our fabricated device was designed with a heated channel length of 6 mm between the air inlet and the Venturi. Simulations of our particular geometry and heater placement that do not assume uniform flow velocity indicate our analytical solution overestimates the entrance length by a factor of two (data not shown).

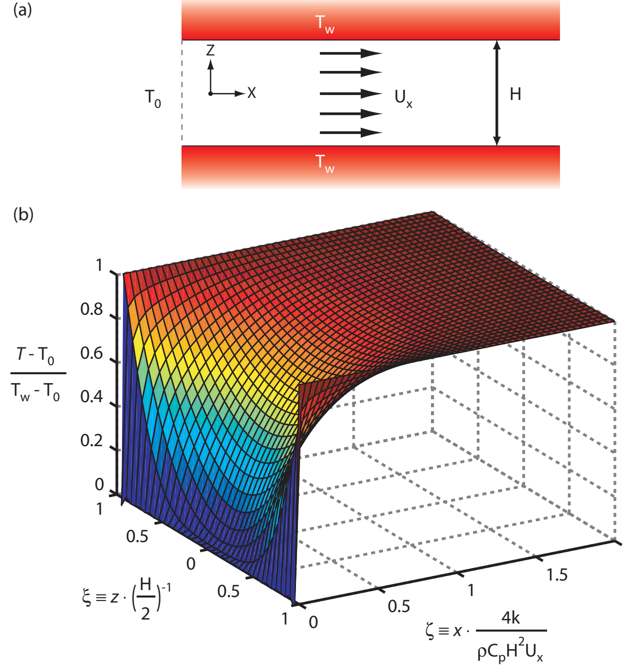

Figure 2.7. Analytical approximation of the axial evolution of the *z*-dimensional temperature gradient. (*a*) The system this solution characterizes is a two-dimensional system in which an incompressible fluid at initial temperature T_0 flows at uniform velocity U_x between two flat walls heated to temperature T_w. Conductive heat transfer in the *x*-direction is assumed negligible, as is convective heat transfer in the *z*-direction. Although the heaters in our device are only located along one wall, the observation that the thermal conductivity of the glass ($k_{Borofloat} = 1.2$ W m^{-1} K^{-1}) exceeds that of air ($k_{air} = 0.026$ W m^{-1} K^{-1}) by two orders of magnitude suggests that the assumption of equal wall temperature is reasonable. Neglecting the *z*-dimensional velocity gradient makes this a worst-case approximation in that heat transfer would be accelerated if this assumption were discarded. (*b*) In this solution, the position variables, ζ and ξ, have been nondimensionalized by the thermal entrance length [$4k_{air}\cdot(\rho_{air}C_pH^2U_x)^{-1}$], which equals 4 mm in our system, and the channel half-height (0.5*H*), respectively. At ζ = 1, the temperature variation is less than 11 percent of the initial temperature difference.

The relationship between constriction pressure and temperature remains linear irrespective of inlet pressure. In Fig. 2.6, we selected inlet pressures such that the middle of the temperature range corresponded to a neutral constriction pressure. Figure 2.8 shows the 80 μm device operated at different inlet pressures. The strength of the temperature dependence and range of output pressures varies slightly with different inlet

pressures. However, the consistent linearity of the Venturi microregulator implies that multiple pressure control ranges, not necessarily restricted to positive/negative switching, can be output by the same microregulator geometry. This expansion of the control range of the Venturi microregulator essentially allows the pressure regulator controlling the air input to the microregulator to serve as a coarse control and the thermal switching mechanism to serve as a fine control in achieving a target output pressure.

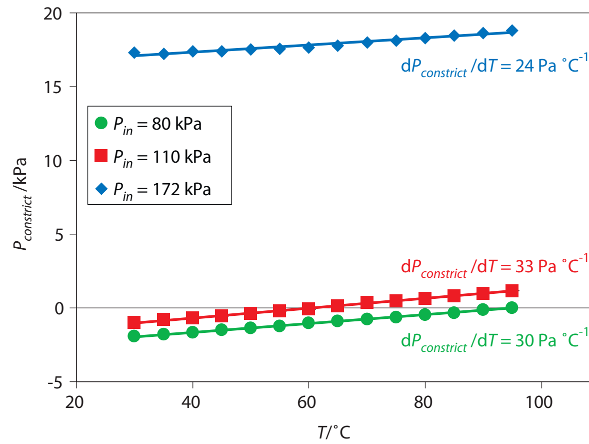

Figure 2.8. Linear variation of constriction pressure with increasing temperature remains consistent over multiple inlet pressures. A microregulator of 80 µm depth is operated at inlet pressures of 80 kPa, 110 kPa, and 172 kPa. The data points in the 80 kPa and 172 kPa series each represent one measurement.

Droplet movement using Venturi pressure microregulator

The pressures generated by the Venturi microregulator are appropriate for controlled liquid droplet motion in microfluidic systems. We fabricated a Venturi microregulator—geometrically identical to Fig. 2.2a but scaled down by a factor of two in all linear dimensions—with a serpentine channel of constant cross-section (550 μm × 76 μm) connected at the sidearm (Fig. 2.9) to demonstrate this application. The inlet pressure of the microregulator was set at 99 kPa, and the heater temperature was initially set to 55°C. A 1 μL droplet of DI H_2O was placed at the liquid inlet to the sidearm channel. With the heater temperature then set to 25°C as shown in Fig. 2.10, the droplet moved toward the microregulator. Setting the temperature back to 55°C halted the droplet. The flow direction reversed when the heater temperature increased to 85°C, and movement could again be stopped by returning the temperature setpoint to 55°C (see movie in supplementary information). The velocity of the drop in either direction was on the order of 1 cm s^{-1}.

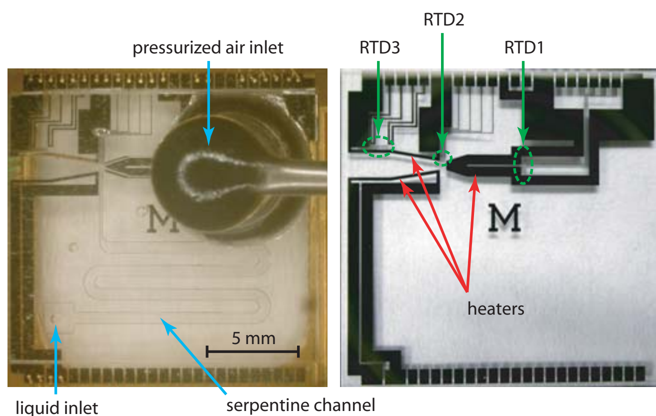

Figure 2.9. Venturi pressure microregulator with constant width (550 μm) serpentine channel attached to sidearm for demonstrating controlled droplet motion. The nozzle geometry is identical to Fig. 2.2a scaled down by a factor of two. The channel depth is 76 μm. The assembled device is shown on the left and the heaters and RTDs are shown on the right.

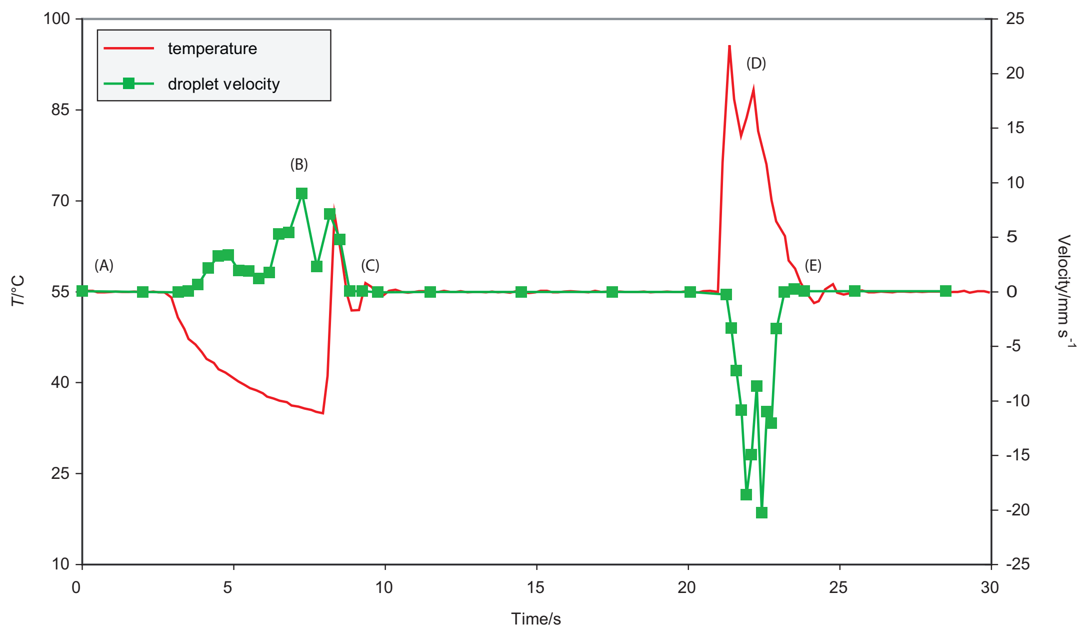

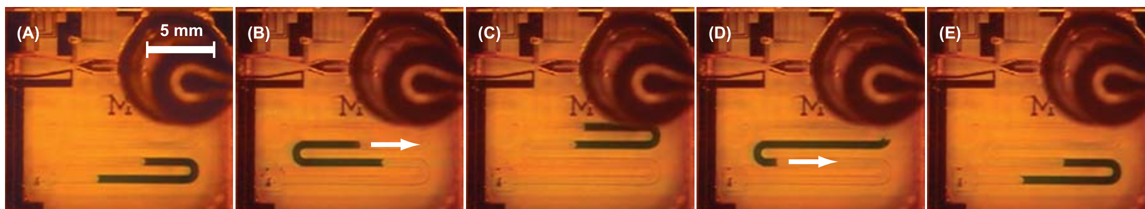

Figure 2.10. Venturi temperature (measured by RTD1 in Fig. 2.9) and droplet velocity plotted over time for one switching cycle. The delay between temperature change and droplet movement is longer for cooling processes than heating processes due to the lack of active cooling and the high thermal capacitance of the glass substrate. Fluctuations in temperature near (*C*) and (*D*) occur when the temperature control algorithm attempts to achieve an instantaneous increase to the setpoint. Fluctuations in velocity occur when the droplet traverses the curves in the sidearm channel, which force the direction of the momentum vector to reverse. Representative images of drop position corresponding to the timepoints: (*A*) 0 s, (*B*) 7.5 s, (*C*) 9.5-21 s, (*D*) 22 s, (*E*) 23 s are shown. Arrows indicate the direction of droplet motion. Positive velocities indicate movement toward the Venturi; negative velocities indicate movement toward the liquid inlet.

As required of any microfluidic flow control mechanism, the Venturi microregulator provides rapid response to permit accurate positioning of droplets. The mean times for droplet deceleration to zero velocity or acceleration to 30 percent of maximum velocity after changing the temperature setpoint was less than 0.8 s for all transitions. The lone exception was the transition from 55°C to 25°C where an average of 1.3 s elapsed between decreasing the temperature setpoint and acceleration of the droplet to 30 percent of maximum velocity. This acceleration response is slower than the other transitions because of the small temperature gradient present. Overall, the absence of active cooling and the high thermal capacitance of the Borofloat glass substrate (C_p = 0.83 kJ kg^{-1} K^{-1} at 20°C-100°C) renders device cooling slower than heating. Incorporation of thermal isolation features and optimization of heater placement would accelerate switching and minimize power consumption by maximizing heat conduction to the working fluid. Peak power consumption in our system at 85°C was 6.75 W but could be reduced with improved thermal isolation toward the theoretical adiabatic minimum of 0.38 W. Thermal isolation also offers the added benefit of suppressing undesired thermal diffusion into regions adjacent to the microregulator with demonstrated temperature gradients as high as 158 °C cm^{-1}.[20]

An interesting phenomenon is that accurate droplet positioning is aided by the existence of a range of temperatures—rather than a single temperature—over which the flow rate falls to zero due to contact angle hysteresis.[21] Fig. 2.10 indicates the liquid velocity has decelerated to zero via the slower 85°C to 55°C transition when the Venturi temperature is still approximately 64°C, delineating the upper bound of the temperature

range for halting drop motion. This phenomenon could be used in conjunction with hydrophobic patterning[22] for sample and reagent metering.

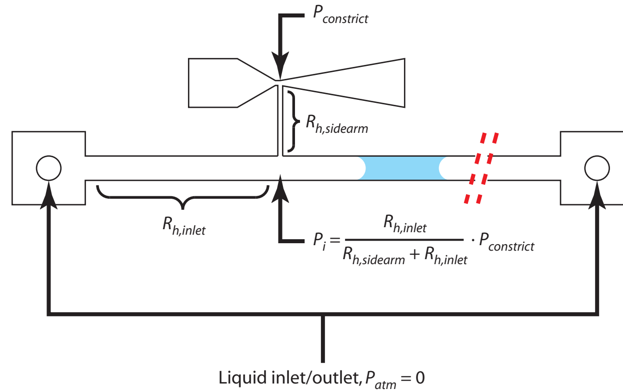

Figure 2.11. Schematic illustrating droplet movement in an open channel system. The fluidic resistances of either the microregulator sidearm or the liquid channels must be appropriately designed to allow the desired range of pressures to be set at P_i. The velocity of the droplet is determined by the pressure difference between its two interfaces. Because the viscosity of the liquid greatly exceeds the viscosity of the air, the pressure at each interface is effectively equal to the pressure at the adjacent channel intersection or inlet/outlet. Additional Venturi microregulators along the channel would increase the spatial resolution with which in-channel pressure gradients could be set and also enable control of branching channel systems.

The droplet movement system can also be used in an open channel network with multiple Venturi microregulators. As opposed to the closed system depicted in Figures 2.9 and 2.10 where one end of the liquid channel is effectively sealed by the microregulator and the pressure difference between the two ends of the droplet is simply equal to $P_{constrict}$, using the Venturi microregulator in an open system would require the microregulator be able to source or sink sufficient air to create the necessary in-channel pressure differences. For instance, the microregulator arrangement in Fig. 2.11 can move the droplet given that a sufficiently large pressure difference, P_i, can be generated, as given by the equation:

$$P_i = \frac{R_{h,inlet}}{R_{h,sidearm} + R_{h,inlet}} P_{constrict} = \frac{D_{h,sidearm}^4 L_{inlet}}{D_{h,inlet}^4 L_{sidearm} + D_{h,sidearm}^4 L_{inlet}} P_{constrict}, \quad (2.4)$$

where R_h is the fluidic resistance defined in Eqn. 2.2. In deriving Eqn. 2.4, the air flow rate between the droplet and the sidearm is assumed to be negligible since the liquid motion is slow relative to the airflow between the sidearm and the left inlet ($\mu_{water} \approx 100\mu_{air}$). Note that expanded designs with multiple microregulators would allow more P_i values to be set at additional points along the liquid channel, easing the requirements on each individual microregulator and enabling fluidic control in branching channels.

Conclusions

This work introduces the concept of electronically controlling the physical parameters of a gas to regulate pressure at ambient conditions. The pressure microregulator we have fabricated and characterized operates exclusively by electronic temperature control, which renders moving parts unnecessary and enables rapid and accurate response. Because this response is linear with input signal (33 Pa °C^{-1}), our microregulator is simple to operate. Although our particular design provides fine control over a 2 kPa output range, alternate designs producing other output ranges should also be possible. These alternatives include departure from the Venturi geometry and utilization of control mechanisms more complex than thermally induced viscosity change, such as ionization of the gas to plasma.

The ostensibly planar nature of microfabrication inherently decouples design of the converging-diverging Venturi nozzle geometry (*xy*-plane) and the thermal switching geometry (*xz*-plane). This decoupling is evident from the observation that the viscous forces acting in the airflow depend primarily on D_h, which is virtually identical to the *z*-dimensional depth of our channels due to their high aspect ratio, while the Venturi effect is manifest due to the difference in cross-sectional area between the inlet and constriction, which is solely due to the difference in *y*-dimensional channel width at each point given the uniform etch depth. We have detailed our experimental characterization of the viscous thermal switching phenomenon and identified the key geometric parameters influencing pressure control range and resolution. However, we have not addressed the design of the Venturi nozzle in our current work. The nozzle geometry depicted in Fig. 2.2a was selected based on approximate two-dimensional simulation results and the

general macroscale Venturi design guideline that the diverging cone angle should be shallower than the converging cone angle for maximum momentum recovery. Optimization of the Venturi geometry would expand the range of the microregulator's control.

The performance of our current Venturi pressure microregulator suggests a number of potential applications. We have demonstrated the use of an integrated Venturi pressure microregulator to move liquid droplets in a microchannel at velocities on the order of 1 cm s^{-1} with the ability to start and stop liquid movement in less than 1 s. One could envision extending this concept to an array of many microregulators for distributed pressure control, each with individually addressable heating elements but all sharing only one common air inlet. Thermal isolation may be needed for closely spaced microregulators or if neighboring components are temperature-sensitive. While our design is readily integrable into most device designs utilizing fluidic channels and electronics without introducing additional fabrication steps, a module containing Venturi microregulators could be interfaced via aligned through-holes to a separate microfluidic device or even serve as a standalone pressure controller. Ultimately, the general utility of this concept extends beyond droplet motion to encompass continuous liquid or gas flows and other applications requiring high resolution pressure control.

References

[1] M. W. Losey, R. J. Jackman, S. L. Firebaugh, M. A. Schmidt and K. F. Jensen, Design and fabrication of microfluidic devices for multiphase mixing and reaction, *J Microelectromech Syst*, 2002, **11**, 709-717.

[2] J. Kobayashi, Y. Mori, K. Okamoto, R. Akiyama, M. Ueno, T. Kitamori and S. Kobayahi, A microfluidic device for conducting gas-liquid-solid hydrogenation reactions, *Science*, 2004, **304**, 1305-1308.

[3] R. S. Besser, X. Ouyang and H. Surangalikar, Hydrocarbon hydrogenation and dehydrogenation reactions in microfabricated catalytic reactors, *Chem Eng Sci*, 2003, **58**, 19-26.

[4] M. Agah, G. R. Lambertus, R. Sacks and K. Wise, High-speed MEMS-based gas chromatography, *J Microelectromech Syst*, 2006, **15**, 1371-1378.

[5] S. I. Ohira and K. Toda, Hybrid microfabricated device for field measurement of atmospheric sulfur dioxide, *Anal Chem*, 2002, **74**, 5890-5896.

[6] D. Erickson and D. Li, Integrated microfuidic devices, *Anal Chim Acta*, 2004, **507**, 11-26.

[7] M. Hashimoto, P. C. Chen, M. W. Mitchell, D. E. Nikitopoulos, S. A. Soper and M. C. Murphy, Rapid PCR in a continuous flow device, *Lab Chip*, 2004, **4**, 638-645.

[8] E. A. Schilling, A. E. Kamholz and P. Yager, Cell lysis and protein extraction in a microfluidic device with detection by a fluorogenic enzyme assay, *Anal Chem*, 2002, **74**, 1798-1804.

[9] R. Pal, M. Yang, R. Lin, B. N. Johnson, N. Srivastava, S. Z. Razzacki, K. J. Chomistek, D. C. Heldsinger, R. M. Haque, V. M. Ugaz, P. K. Thwar, Z. Chen, K. Alfano, M. B. Yim, M. Krishnan, A. O. Fuller, R. G. Larson, D. T. Burke and M. A. Burns, An integrated microfluidic device for influenza and other genetic analyses, *Lab Chip*, 2005, **5**, 1024-1032.

[10] R. G. Blazej, P. Kumaresan and R. A. Mathies, Microfabricated bioprocessor for integrated nanoliter-scale Sanger DNA sequencing, *Proc Natl Acad Sci USA*, 2006, **103**, 7240-7245.

[11] R. L. Chien and J. W. Parce, Multiport flow-control system for lab-on-a-chip microfluidic devices, *Fresenius J Anal Chem*, 2001, **371**, 106-111.

[12] M. A. Eddings and B. K. Gale, A PDMS-based gas permeation pump for on-chip fluid handling in microfluidic devices, *J Micromech Microeng*, 2006, **16**, 2396-2402.

[13] M. A. Unger, H. P. Chou, T. Thorsen, A. Scherer and S. R. Quake, Monolithic microfabricated valves and pumps by multilayer soft lithography, *Science*, 2000, **288**, 113-116.

[14] C. H. Wang, and G. B. Lee, Pneumatically driven peristaltic micropumps utilizing serpentine-shape channels, *J Micromech Microeng*, 2006, **16**, 341-348.

[15] K. Handique, D. T. Burke, C. H. Mastrangelo and M. A. Burns, On-chip thermopneumatic pressure for discrete drop pumping, *Anal Chem*, 2001, **73**, 1831-1838.

[16] S. McNamara and Y. B. Gianchandani, On-chip vacuum generated by a micromachined Knudsen pump, *J Microelectromech Syst*, 2005, **14**, 741-746.

[17] C. K. Chung, W. J. Chang, Y. F. Kuo, C. L. Hsiao and K. Y. Weng, Pneumatically bidirectional microfluidic regulation using Venturi pumps by deep RIE and bonding technology, *Microsyst Technol*, 2002, **8**, 318-322.

[18] J. West and A. Jadhav, ECDM methods for fluidic interfacing through thin glass substrates and the formation of spherical microcavities, *J Micromech Microeng*, 2007, **17**, 403-409.

[19] J. D. Anderson, in *Modern Compressible Flow with Historical Perspective*, ed. J. D. Anderson, McGraw Hill, Boston, 3rd edn., 2003, ch. 5, pp. 202-211.

[20] M. Yang, R. Pal and M. A. Burns, Cost-effective thermal isolation techniques for use on microfabricated DNA amplification and analysis devices, *J Micromech Microeng*, 2005, **15**, 221-230.

[21] T. S. Sammarco and M. A. Burns, Thermocapillary pumping of discrete drops in microfabricated analysis devices, *AIChE J*, 1999, **45**, 350-366.

[22] K. Handique, D. T. Burke, C. H. Mastrangelo and M. A. Burns, Nanoliter liquid metering in microchannels using hydrophobic patterns, *Anal Chem*, 2000, **72**, 4100-4109.

CHAPTER 3

A VENTURI MICROREGULATOR ARRAY MODULE FOR DISTRIBUTED PRESSURE CONTROL

Introduction

Pressure-driven flow control systems in lab-on-a-chip devices have long been a compromise between design modularity and ease of implementation. For example, passive flow control schemes relying on capillary forces[1,2,3,4,5] or centrifugal actuation[6,7,8,9] are attractive, particularly for portable devices, due to their straightforward fabrication and minimal dependence on external supporting infrastructure. But unlike modular reaction or detection components that can typically be swapped into new device designs with little modification, valve dimensions and channel geometries of passive flow control systems must be tailored to application-specific combinations of fluid, substrate, and desired flow pattern. Conversely, fully integrated micropump[10] and microvalve[11,12] designs in active flow control schemes are highly modular and can essentially be copied and pasted between device layouts. However, this improvement incurs the costs of increased fabrication complexity and potential structural fatigue associated with moving parts inherent to mechanical components. The tremendous popularity of pneumatically controlled microvalves[13] is largely attributable to their comparatively simple fabrication through the use of off-chip solenoid valve arrays in place of on-chip actuators. This versatile design has proven suitable for a wide variety of applications but does not scale

favorably with increasing numbers of valves due to the individual connection necessary to interface each external control component. Similar scalability considerations apply to direct pressure systems utilizing syringe pumps or external pressure controllers.

The type of flow control selected also determines whether the channel network to be controlled operates as "open" or "closed." We can think of the majority of microfluidic systems as closed networks in which mechanical barriers push fluid or direct flow. These systems use either integrated or external in-line pumps to displace one or more continuous streams of fluid at prescribed flow rates. In contrast, we will refer to an open channel network as a system of microchannels devoid of mechanical valves or seals for directing fluid flow. In this case, flow control relies on specific pressures imposed at key locations. These pressures can result from differences in capillary pressure or centrifugal force in passive flow control systems or applied pressure gradients in actively controlled systems. Open channel networks are ideal for droplet-based systems—characterized by transport of discrete fluid volumes to specific positions at specific times—in which flow rates are typically inconsequential.

Toward development of a modular active flow control platform, we describe the design and demonstrate the application of a multiplexed Venturi microregulator array for droplet manipulation in an open microchannel network via distributed pressure control. Previously published work by our group introduced the Venturi microregulator (Fig. 3.1c) as a high-resolution pressure controller, readily integrable in existing microfluidic device designs.[14] The microregulator consists of pressurized gas flowing through a converging-diverging nozzle with a sidearm connected at the nozzle constriction. Modification of the gas temperature using microfabricated heating elements perturbs the

flow to enable switching of the sidearm output between positive and negative gauge pressure. The highly modular design potentially allows any number of arrayed Venturi microregulators, each capable of outputting an independently controlled pressure, to share a single pressure input, resulting in a compact unit uniquely suited for distributed pressure control. Such a unit, directly interfaced to a microfluidic device in a multilayer structure, would require no additional external fluidic connections and possess no moving parts.

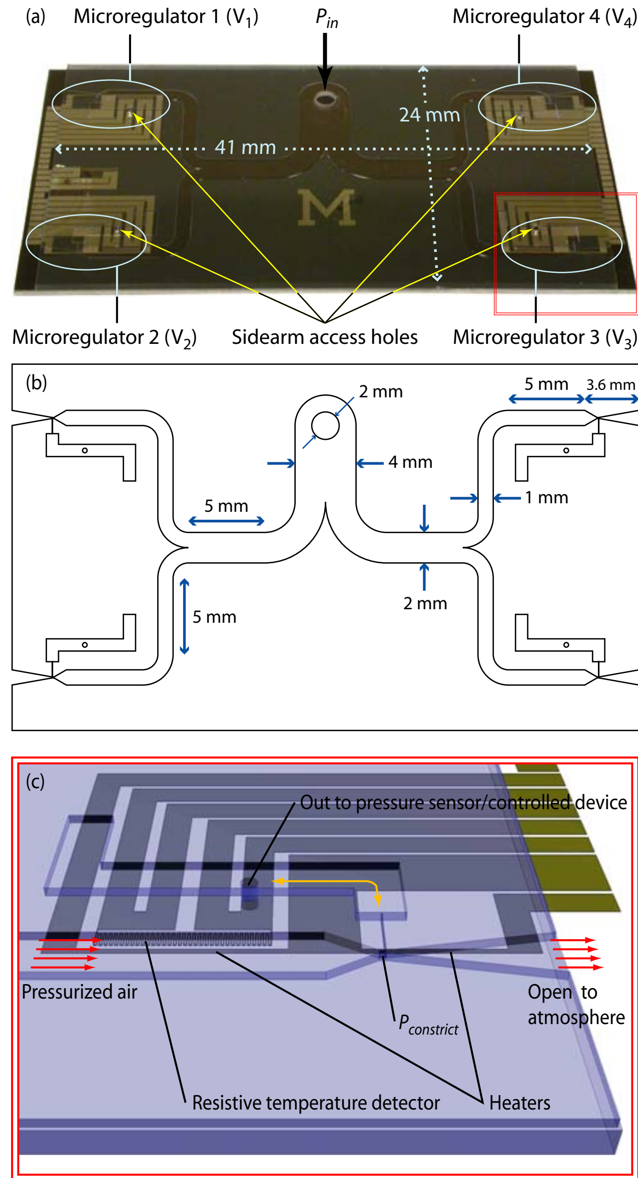

Figure 3.1: Multiple Venturi microregulator module. (*a*) Arrayed Venturi microregulator module investigated in our current work. Four microregulators share one pressure inlet set at a constant inlet pressure, P_{in}, and are numbered from one to four proceeding counterclockwise from the upper left. (*b*) Dimensions of array geometry. Constriction width is approximately 130 μm. Width of sidearm connected to constriction is approximately 86 μm. Converging and diverging angles of the nozzles are 30° and 10°, respectively. Etch depth is 76 μm. (*c*) Inset showing single microregulator schematic. Heating the air flow through the converging-diverging channel increases the constriction pressure output through the access hole in the sidearm ($P_{\text{constrict}}$).

Materials and methods

Venturi microregulator array fabrication

The Venturi microregulator array devices consist of an upper glass piece etched with the array geometry anodically bonded to a lower silicon piece patterned with the heaters and four-point resistive temperature detectors (RTDs). Figure 3.2 shows the fabrication process. The array geometry was etched to a depth of 76 μm in Borofloat glass wafers (700 μm thick, 10 cm diameter) using standard photolithography and hydrofluoric acid wet etch techniques. The isotropic wet etch leads to a trapezoidal channel profile with a lateral etch equal to the depth of the channel. Pressure inlet holes (designated P_{in} in Fig. 3.1a) were drilled using a high-speed drill press with a diamond-tipped bit (1.5 mm diameter; UKAM Industrial Superhard Tools, Valencia, CA). Smaller sidearm access holes (identified in Fig. 3.1a) of 0.5 mm diameter were drilled by electrochemical discharge machining.

Heaters and RTDs on the lower silicon piece were patterned in a single metal layer using a standard liftoff process. Bare silicon wafers (550 μm thick, 10 cm diameter) coated with a 100 nm thermal oxide were lithographically processed. Titanium and platinum (300/1000 Å) were evaporated onto the patterned wafer. The wafer was sonicated in acetone for 10 min to lift off unwanted metal. The measured resistances were approximately between 50 Ω and 100 Ω (heaters) and 2000 Ω (RTDs).

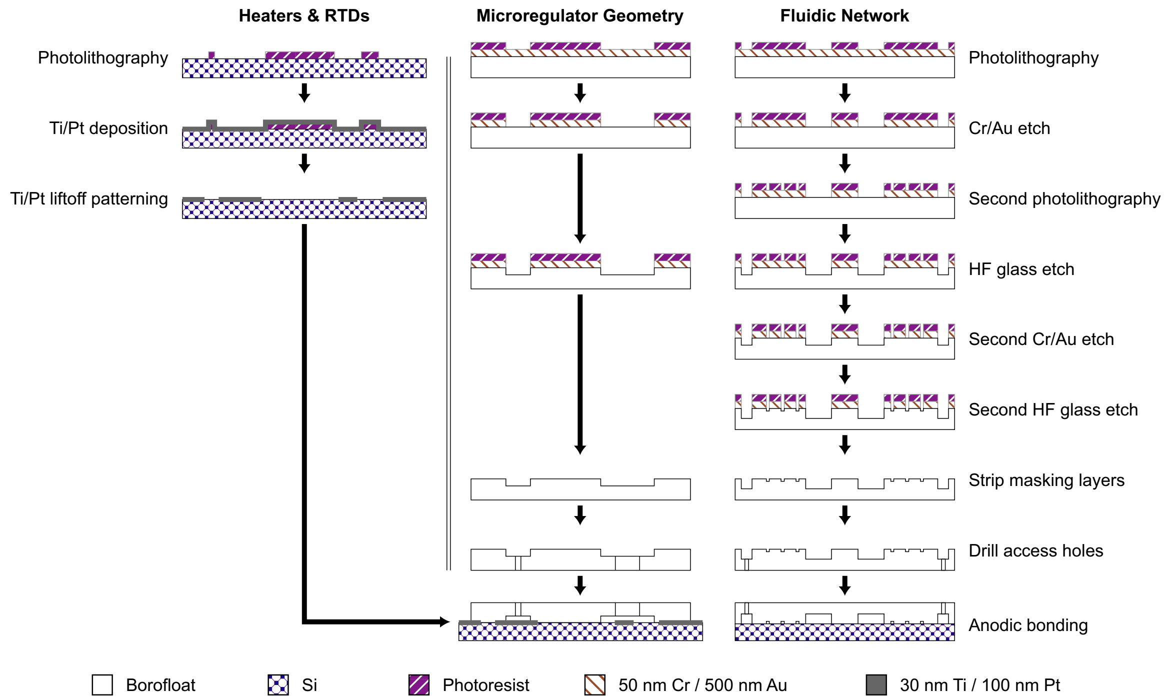

Figure 3.2: Fabrication process flow. Fabrication of the fluidic network uses two etches to generate the deep main channels and the shallow inlet channels, which are labeled R_{inlet} in Fig. 3.8c.

The glass and silicon wafers were cleaned, anodically bonded, and diced. In preparation for bonding, the etched glass wafer was cleaned in piranha solution, and both wafers were sonicated in acetone and isopropanol. The wafers were then aligned by eye and anodically bonded at 350 °C and 1000 V. After bonding, the wafers were diced to expose the electrical contact pads and to obtain the individual devices. Each device was affixed using standard quick cure epoxy and wire bonded to a printed circuit board. Syringe tips (Part Number 5114-B-90; EFD Inc., East Providence, RI) glued to glass capillaries (2 mm I.D.) were attached to the inlet holes with epoxy (Steel Weld Epoxy; ITW Performance Polymers, Riviera Beach, FL) for interfacing to off-chip connections. Geometric tuning was performed by selectively sealing the tuning ports using the same epoxy.

Open fluidic network fabrication

The open microchannel network devices also consist of an etched upper glass piece anodically bonded to a lower silicon piece. To generate a geometry containing two distinct etch depths, Borofloat glass wafers coated with chromium and gold (500/5000 Å) were lithographically patterned (Microposit SC 1827; Shipley Co., Marlborough, MA) to expose a set of deep features from which the metal was removed. The wafer was then exposed and developed a second time to pattern a set of shallow features (designated R_{inlet} in Fig. 3.8c); the metal covering the shallow features was not removed. The wafer was isotropically wet etched in hydrofluidic acid to a depth of 70 μm. The metal covering the shallow features was then etched away. The wafer was etched a second time to achieve a depth of 30 μm in the shallow features and a total depth of 100 μm in the deep features. After stripping the remaining metal and photoresist, inlet holes were drilled by electrochemical discharge machining. The wafer was then cleaned, anodically bonded to a bare silicon wafer, and diced as previously described. Syringe tips and glass capillaries were attached to allow interfacing to the microregulator array device using silicone tubing (1.6 mm I.D.). Channel surfaces were hydrophobically treated before use (Rain-X Original Glass Treatment; SOPUS Products, Houston, TX).

Device operation

Lab air supply, controlled by a pressure regulator (Model Number 3476A; Matheson Gas Products Inc, Irving, TX), was continuously fed to the gas inlet of the device. The heaters and RTDs on the device were controlled by a DC power supply (Model Number HY5003; Mastech, Hong Kong), two data acquisition (DAQ) boards (PCI-6031E and PCI-6704; National Instruments, Austin, TX), two connector blocks (SCB-100 and SCB-68; National Instruments), a custom signal conditioning circuit, a computer, and a LabVIEW program (National Instruments). To calibrate the thermal sensors, the entire device was heated in a convection oven whose temperature was ramped from room temperature to 100 °C. Simultaneously, a current of 3 mA was sent through two leads of the four-point RTDs while the voltage across the other two leads was recorded in a LabVIEW program. Once converted to resistance, a linear fit of the resistance and temperature data was generated. A proportional-integral control algorithm used in conjunction with this linear fit regulated the voltage across the microfabricated heaters, enabling feedback control of each heater (± 0.5 °C) via the closest RTD. All constriction pressure measurements were serially recorded using an electronic pressure sensor (± 10 Pa, Strain Gage Panel Meter DP25B-S; Omega, Stamford, CT) connected to the sidearm access hole. Measurements were recorded after the constriction pressure stabilized at a steady state value following any change in temperature or inlet pressure. Sealing or unsealing of the other sidearm access holes while measuring the constriction pressure of any one microregulator had no effect on the measurement.

Results and discussion

Geometric design and tuning

Uniform microregulator behavior throughout the array is a critical requirement for distributed pressure control. Any deviation in constriction pressure among arrayed microregulators operated at the same temperature and inlet pressure is almost exclusively attributable to non-uniformities in flow geometry. Because the intended control range of the constriction pressure ($P_{constrict}$ ~ 1 kPa) is two orders of magnitude smaller than the total pressure drop through the Venturi nozzle (P_{in} ~ 200 kPa), inhomogeneities in the etched surface and minor flow perturbations may result in unacceptably large deviations in constriction pressure that are not time-dependent. Minimizing this deviation eliminates pressure gradients between microregulators set at identical temperatures. Although thermally suppressing such deviations is possible by independently setting each microregulator to its respective neutral temperature (i.e., temperature resulting in $P_{constrict}$ = 0), solely relying on this strategy can impose large fixed temperature offsets and drastically reduce the available control range of the individual microregulators. Consideration of flow geometry during device design and incorporation of features enabling post-fabrication tuning of the flow geometry significantly improve constriction pressure uniformity.

Asymmetric flow splitting is one major source of constriction pressure variability. The flow profile through the Venturi nozzle dictates the constriction pressure of a microregulator; therefore, the behavior of individual microregulators will not be identical unless the streamlines through each microregulator are identical. Figure 3.3a depicts a

compact “out-of-plane” flow splitting geometry, in which the flow is forced to the arrayed microregulators immediately upon entering the device. All three components of the velocity vector are nonzero at the point the entering fluid simultaneously impinges on the floor of the device and begins to divide toward each of the four microregulators, rendering the flow particularly susceptible to uneven splitting due to minor perturbations. The geometry in Fig. 3.3b partially remedies this problem by restricting all flow splitting to the same plane such that the z-dimensional velocity is negligible but necessitates the use of a binary-tree layout to maintain streamline symmetry. Based on simulation data (not shown), the length of channel required to reestablish a uniform velocity profile after a bend or split in a constant cross-sectional area channel is approximately 2 cm for our etch depth of 76 µm. Because inclusion of a 2 cm straight channel segment upstream of each branch point would make the total area of the device impractically large, we devised an alternative method for geometrically reducing the constriction pressure variability.

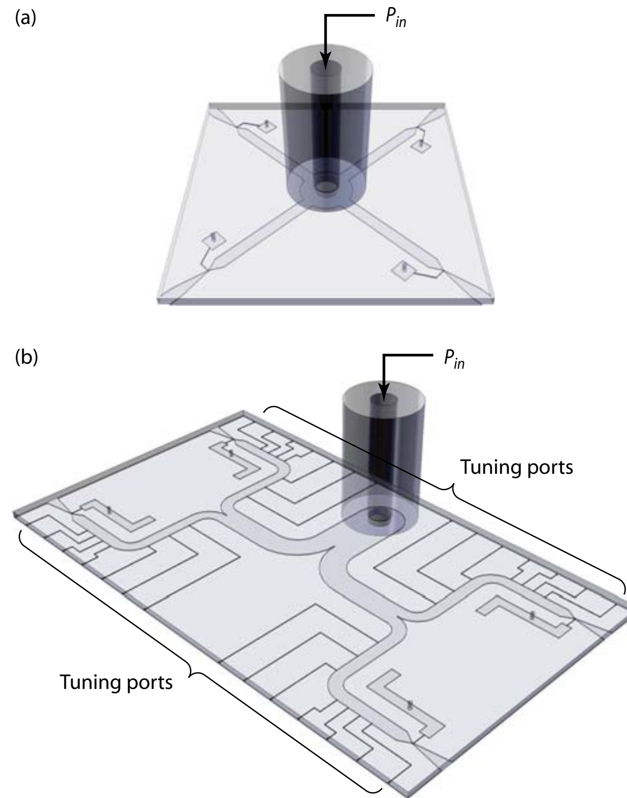

Figure 3.3: Alternate microregulator array geometries. (*a*) Out-of-plane flow splitting geometry. (*b*) Microregulator array with tuning ports for post-fabrication modification of the flow geometry. Fabricated tuning ports are approximately 86 μm wide. Each tuning port can be sealed to locally increase the pressure in its respective branch.

Geometric suppression of constriction pressure variability can be achieved by empirical, post-fabrication tuning via additional tuning ports as illustrated in Fig. 3.3b. The tuning ports function as bleed valves that can be individually sealed to effectively increase the inlet pressure of any one microregulator relative to the others as shown in Fig. 3.4. Because the tuning process translates the curves of Fig. 3.4 along the abscissa without changing the shapes of the curves, device calibration enables constriction pressure matching at one inlet pressure. In practice, the tuning procedure is a one-time task after which the constriction pressures remain matched for the lifetime of the device; we have not observed any notable change in constriction pressure matching after four months of use.

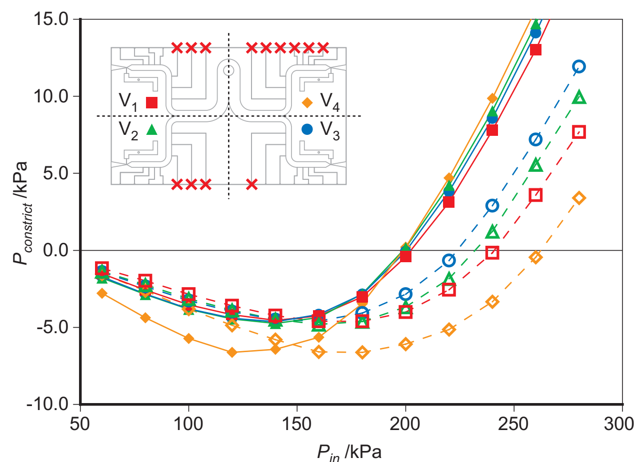

Figure 3.4: Plot of constriction pressure behavior with varying inlet pressure at room temperature before (open symbols) and after (filled symbols) geometric tuning, which allows constriction pressure matching at the desired inlet pressure. The final tuning port sealing configuration of the tuned device is shown. Pressure values are in gauge pressure.

“In-plane” flow splitting combined with post-fabrication tuning can achieve a ten times reduction in constriction pressure variability as shown in Fig. 3.5. Figure 3.5 also shows the constriction pressure variability of a silicon device fabricated using deep reactive ion etching (DRIE) and anodically bonded to a glass substrate. Whereas our wet etched glass channels exhibited surface roughness values up to 5%, DRIE typically produces relatively smooth sidewalls with a surface roughness of ≈ 0.5%.[15] This reduction in overall surface roughness appears to have no appreciable effect on constriction pressure variability.

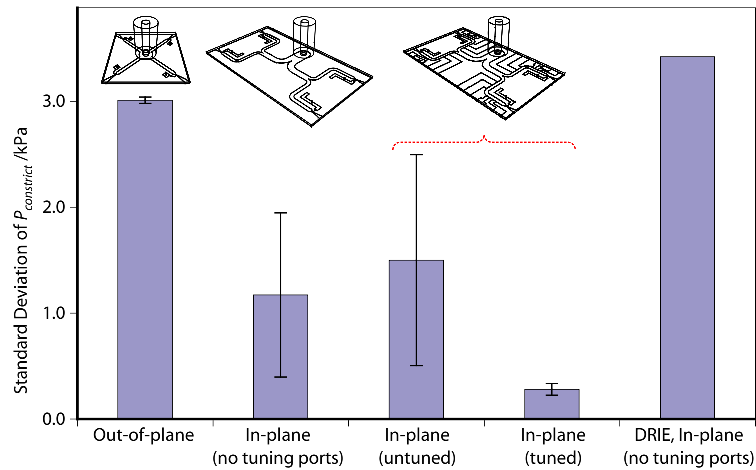

Figure 3.5: Graph of variation among the constriction pressures of arrayed microregulators in different device types. All devices were fabricated in glass except for “DRIE, In-plane,” which was fabricated by deep reactive ion etching in Si. All devices were etched to a depth of 76 μm. The inlet pressure of each device was set such that the mean constriction pressure of the arrayed microregulators equaled zero. The standard deviation among the four microregulators of each device was calculated. The average standard deviation of no fewer than three devices is shown for all device types except “DRIE, In-plane,” for which only one device was tested. Error bars indicate one standard deviation above and below this average.

Multiple microregulator operation

The relationship among constriction pressures of arrayed microregulators is best characterized as a series of differences between the microregulator temperature and a reference temperature rather than simply an absolute temperature. As the Venturi nozzle portion of the microregulator is heated, the combined effects of increased gas viscosity and decreased mass flow, causing the constriction pressure to increase. The exhibited linear dependence, as shown in Fig. 3.6, is identical to the previously reported behavior of a single microregulator. Although the device used to generate the data in Fig. 3.6 has been geometrically tuned, variability among the constriction pressures of the individual microregulators still exists at any given temperature due to the coarseness of the discrete adjustments permitted by the tuning ports. If we define a set of reference temperatures $\{T_{0,i}\}$ corresponding to the neutral temperature of each microregulator, the microregulator pressures can be perfectly matched by mapping constriction pressure as an offset from $T_{0,i}$, represented as ΔT_i. For the device in Fig. 3.6, this produces

$$\left\{\begin{matrix} T_{0,\text{Venturi 1}} = 41\,^{\circ}\text{C} \\ T_{0,\text{Venturi 2}} = 63\,^{\circ}\text{C} \\ T_{0,\text{Venturi 3}} = 51\,^{\circ}\text{C} \\ T_{0,\text{Venturi 4}} = 51\,^{\circ}\text{C} \end{matrix}\right\}.$$

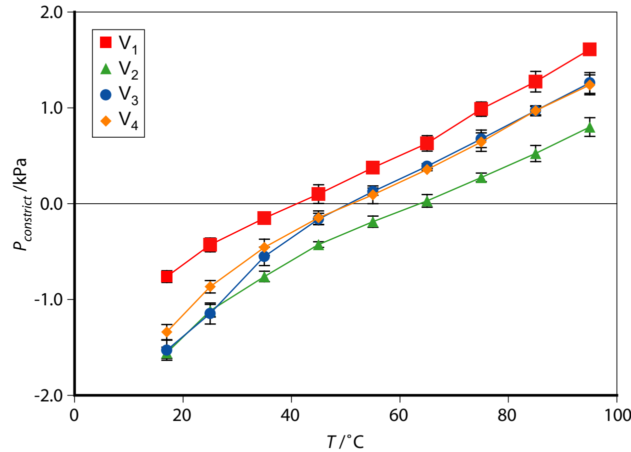

Figure 3.6: Variation of constriction pressure with microregulator temperature in a geometrically tuned device at P_{in} = 200 kPa. Measurements were taken with the indicated microregulator heated to the indicated temperature while all other microregulators were unheated. Although the curves are parallel, they do not perfectly overlap due to the coarseness of the adjustments afforded by the tuning ports. Error bars indicate one standard deviation above and below the mean of triplicate measurements. Pressure values are in gauge pressure.

Thermal crosstalk is an important consideration in designing arrayed microregulators. Thermal diffusion to a microregulator from a neighboring microregulator operated at a higher temperature increases the minimum achievable temperature in the cooler microregulator and consequently decreases the available temperature control range and thus the constriction pressure range. Figure 3.7 shows that thermal diffusion from heated microregulators may prevent neighboring microregulators from reaching their respective desired constriction pressures. The improved positioning of the heating element along the centerline of the Venturi nozzle in the current microregulator design maximizes heater contact with the gas flow, thereby minimizing heat transfer into the substrate and channel walls. Selective active cooling of the device would enable temperature differentials as high as 108 °C cm^{-1} to be sustained between microregulators at the expense of increased power consumption. Alternatively,

suppression of heat transfer away from the Venturi nozzle by increasing the local thermal resistance of the substrate using backside etching could increase the maximum achievable temperature gradient to 158 °C cm^{-1} with decreased power consumption at the expense of added fabrication complexity.[16]

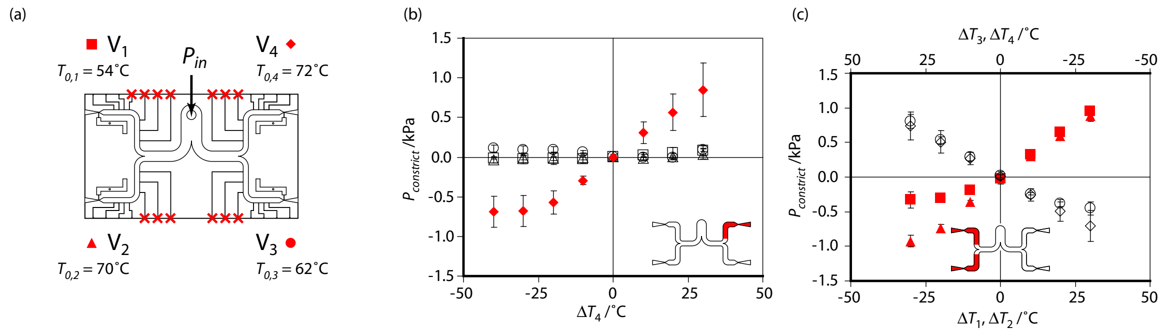

Figure 3.7: Effect of thermal and pressure crosstalk. Thermal crosstalk and the lack of active cooling may render low ΔT setpoints unachievable, resulting in the observed nonlinear variation in $P_{\text{constrict}}$. This is particularly problematic for microregulators with low $T_{0,\text{i}}$ values, where $T_{0,\text{i}}$ is the temperature corresponding to neutral pressure output for microregulator i. ΔT_{i} is the difference between the temperature setpoint of microregulator i and $T_{0,\text{i}}$. (*a*) Tuning port sealing configuration and microregulator designations. (*b*) ΔT_4 is varied while all other microregulators are maintained at $\Delta T = 0$. (*c*) ΔT_1 and ΔT_2 are varied oppositely of ΔT_3 and ΔT_4. This is the maximum achievable pressure difference. Error bars indicate one standard deviation above and below the mean of triplicate measurements. All pressure values are in gauge pressure.

In addition to thermal crosstalk, independent perturbation of the gas flow through any one microregulator should result in minimal upstream interaction that could alter flow through or constriction pressures of other microregulators in the array. Figure 3.7b depicts the constriction pressures of three microregulators maintained at $\Delta T = 0$ while varying the temperature of the fourth microregulator. Interestingly, the constriction pressure of the neutral microregulators appears to weakly vary opposite to that of the active microregulators. This trend contradicts expected variation from thermal crosstalk, suggesting instead that changing the mass flow rate through one microregulator leads to

an opposite change in mass flow rate through the other microregulators and subsequently, an opposite change in constriction pressure. We suspect this may occur due to nonuniform heating in the presence of large temperature gradients, which increases heat transfer into the substrate while decreasing heat transfer into the gas flow and ultimately increases the difference between the heater temperature and the actual temperature of the gas flow.

Fluid manipulation in open microchannel network

Open channel networks intended for distributed pressure flow control should contain appropriately placed fluidic resistances to maximize pressure gradients achievable in the network. Of particular importance is the configuration of the sample inlet region as depicted for our test device in Fig. 3.8. The sample inlet is always open such that the pressure at node A_i is equal to atmospheric. Node V_i is connected to the controlled pressure source—in this case, one microregulator in our Venturi microregulator array. This design results in a maximum (or minimum) achievable pressure at node B_i equal to

$$P_{Bi} = P_{Vi}^{*} \times \frac{R_{inlet}}{R_{inlet} + R_{sidearm}}$$

where P^{*}_{Vi} is the maximum (or minimum) possible pressure output of the microregulator. As R_{inlet} increases, this maximum approaches P^{*}_{Vi}, corresponding to a closed channel network in the limit as $R_{inlet} \rightarrow \infty$. Therefore, bounding the interior nodes of an open channel network with large hydraulic resistances shields the interior of the network from the open exterior nodes fixed at atmospheric pressure.

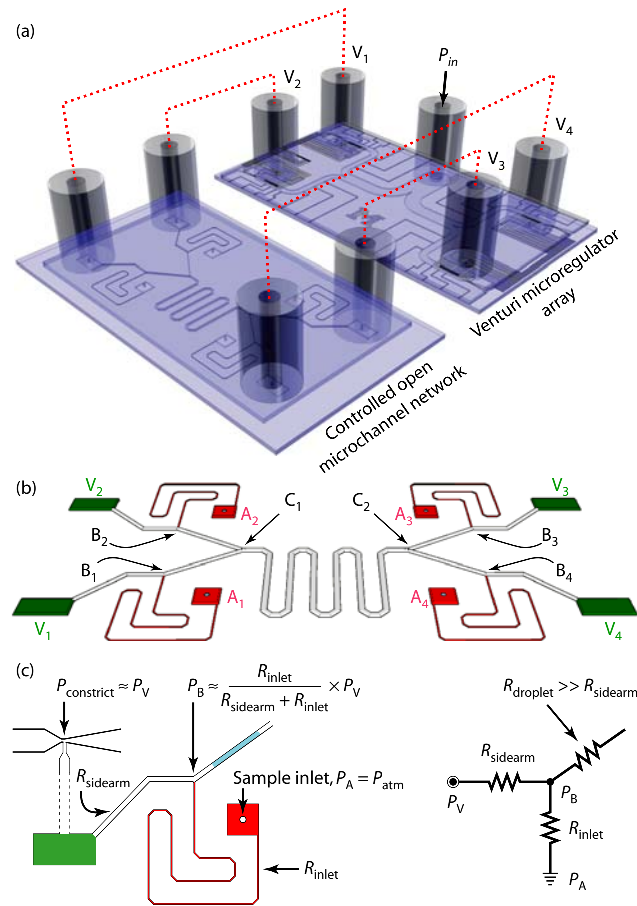

Figure 3.8: Schematic of fluidic network controlled by microregulator array. (*a*) Drawing of experimental system. The microregulator array and the controlled fluidic device are separate devices in the current setup. (*b*) Layout of controlled microchannel network. Nodes A_i are loading ports that are always open to atmospheric pressure. Nodes V_i are connected to the Venturi microregulators. (*c*) Fluidic resistances and electrical circuit equivalent of inlet region. High inlet resistance, R_{inlet}, and low sidearm resistance, $R_{sidearm}$, maximize the range of pressures that can be achieved in the network. $R_{inlet} \approx 180\ R_{sidearm}$ in tested device.

The microfluidic flow control capabilities of the Venturi microregulator array are well illustrated by several operations performed in a separate model device, including droplet loading, movement, splitting, and merging. Figure 3.9 shows the sequence of microregulator settings used to carry out each operation. For example, droplet loading involved setting all microregulators to negative pressure until the desired volume of liquid was drawn in through the inlet. The microregulator closest to the loading inlet was then set to positive pressure to shear the droplet away from the loading channel. The small hydraulic diameter of the high-resistance loading channel ($D_h \approx 32$ μm) causes some degree of self-sealing after droplet loading. The abrupt increases in cross-sectional area at both ends of the inlet channel produce a negative capillary pressure within the residual liquid column. Because contact angle hysteresis demands a higher pressure to expel this column than to move droplets in the larger main channels ($D_h \approx 117$ μm), the residual liquid further helps to shield the network interior. To prevent undesired introduction of air from disrupting droplet cohesion (Fig. 3.9: Single droplet loading), the decreasing pressure gradient from node C_1 to node B_1 is reduced as the droplet begins to pass C_1 to draw a small amount of liquid into the C_1-B_1 channel segment. This weak pressure gradient is reversed once half the droplet has passed C_1 to restore the diverted liquid volume to the main body of the droplet. It is important to note that the specific microregulator settings in Fig. 3.9 are not unique "solutions" for the fluidic manipulations shown. Pressure differences between nodes are responsible for fluid motion; therefore, the pressure at any given node is irrelevant as long as the necessary pressure gradient is maintained.

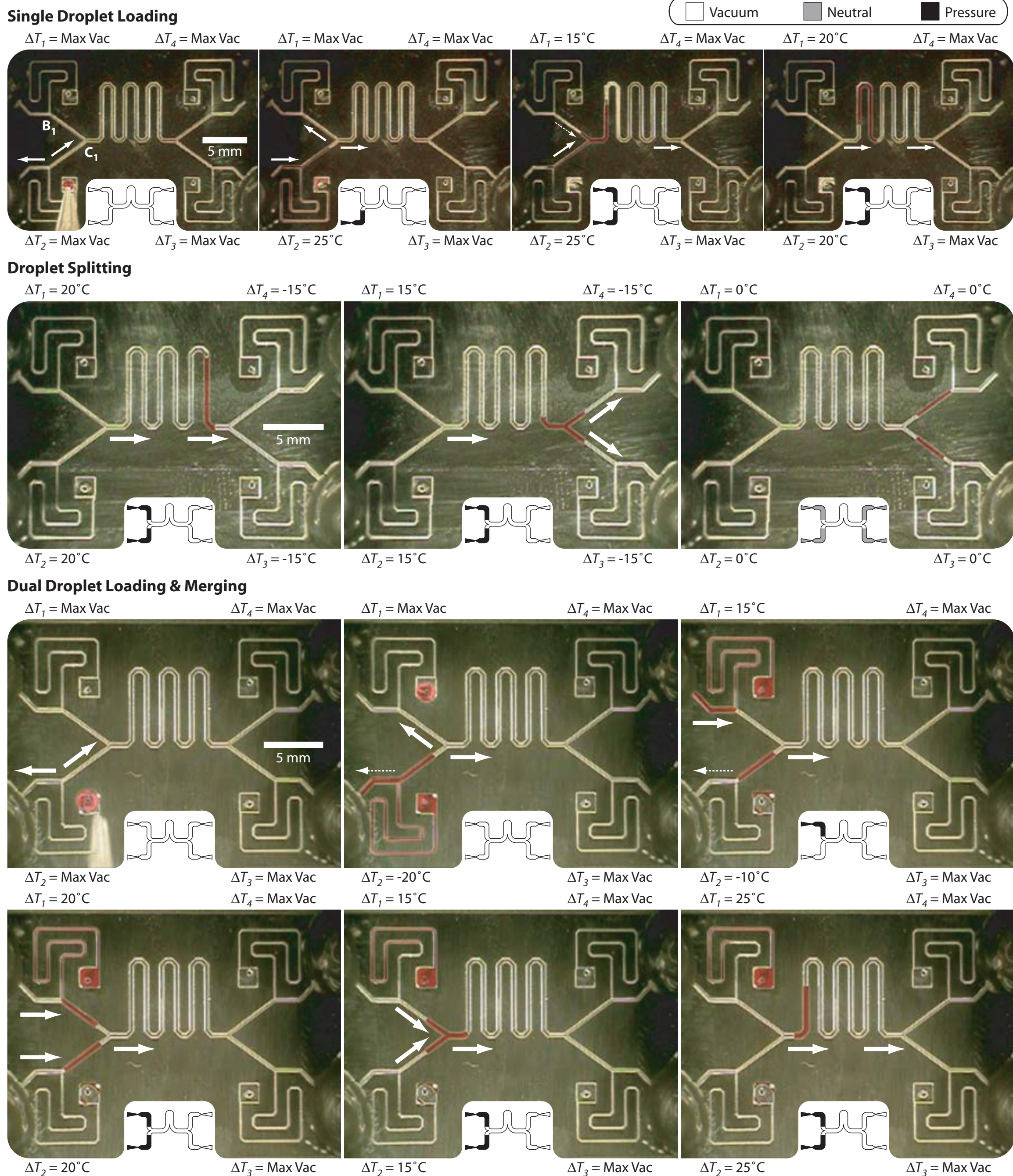

Figure 3.9: Images of various droplet manipulations carried out in fluidic network pictured in Fig. 3.8. Insets show configuration of controlling microregulator array; array orientation is identical to fluidic network orientation (i.e., each microregulator connects to the correspondingly positioned outer control node). ΔT_i is the temperature setpoint of microregulator *i*. *Max Vac* indicates the heaters for that microregulator are turned off to generate maximum vacuum output. Arrows indicate direction of negative pressure gradient; dashed arrows indicate weak pressure gradient. Images recolored.

Barring surface tension effects, the flow rate in any channel segment is zero if and only if no pressure gradient exists down the length of that segment. Because an open channel system does not contain mechanical valves, a zero flow condition in any region of the network is only achieved if the pressures at all bounding nodes are identical. A few specific fluidic manipulations, particularly the simultaneous handling of multiple droplets, highlight the implications of this observation. Figure 3.10 shows several images in which one droplet is moved while holding a second droplet stationary. Because the viscosity of the liquid is two orders of magnitude greater than the viscosity of air, nearly the entire pressure gradient in a channel segment containing any portion of a droplet occurs over the length of the liquid column. The pressure distribution in the network is thus dependent on the position of the droplet. In Fig. 3.10, ΔT_4 is increased as the moving droplet passes node C_2 to match the pressures and prevent flow between nodes B_4 and C_2, keeping the stationary droplet still. If the surface tension of the liquid is sufficient, contact angle hysteresis will negate the effect of small pressure differences, suppressing undesired droplet movement even if the pressures at nodes B_4 and C_2 are not perfectly matched.

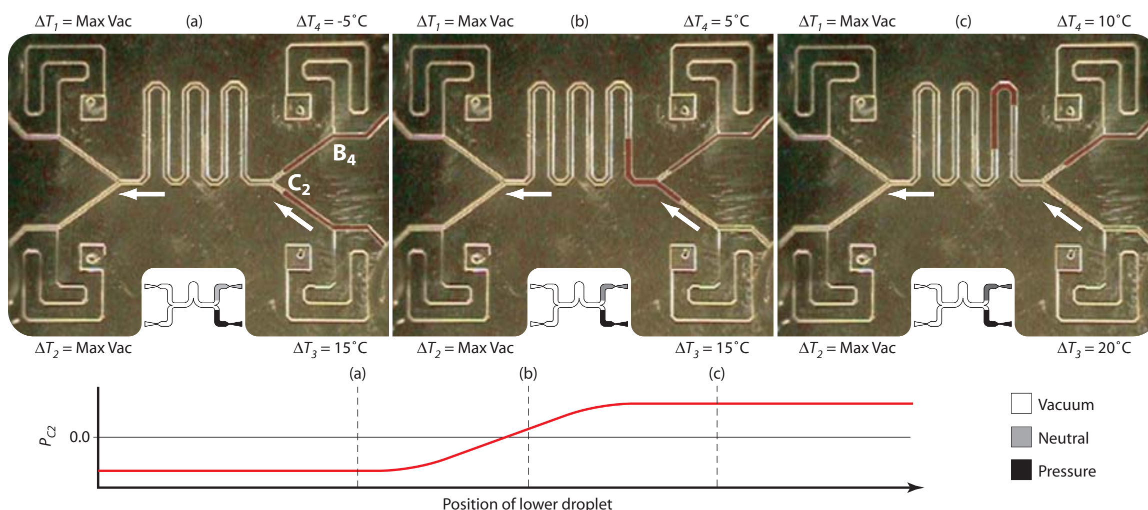

Figure 3.10: Moving one droplet while keeping a second droplet stationary. A zero flow condition between nodes B_4 and C_2 must be maintained to keep the upper droplet still. ΔT_4 is increased as the lower droplet moves past C_2 so the pressures at B_4 and C_2 remain matched. A plot of the relative pressure change at node C_2 is shown. Images are recolored to enhance droplet visibility.

Consistent with the previously reported behavior of single Venturi microregulators, the response time of the microregulator array for halting droplet movement was approximately 0.8 s when all microregulators were reset to neutral pressure, enabling precise droplet positioning. In the current work, movement of droplets beyond their intended positions was not unusual due to insufficiently rapid manual operator response. Feedback control, coupling electrodes for droplet detection and automated control of the microregulator array temperatures, would alleviate this problem as well as significantly reduce the duration of each operation. One possible implementation would use electrodes situated around each node as “tripwires” to detect droplet position.[17,18] In this arrangement, the starting position of the droplet and detection of the droplet’s arrival at the desired ending position are necessary to determine the required modifications in the network pressure distribution to perform a given operation. Additional droplet detection electrodes would also be needed at intermediate branch

points in complex microchannel networks. Based on droplet acceleration and deceleration times reported in our previous work, operations such as droplet merging and splitting would theoretically require less than 5 s in a fully automated system.

Conclusion

Building upon our previous Venturi microregulator design, we demonstrated the independent operation of multiple arrayed microregulators fed by a single pressure source. By using the array to impose arbitrary pressure distributions across a microchannel network, we demonstrated the ability to use such an array as a modular microfluidic flow controller. Although our current implementation consists of the microregulator array and the controlled fluidic network as two separate devices, Fig. 3.11 shows a prototype that integrates the two parts into one multilayer structure. In addition to being a challenge in array scaling and maximization of the pressure control range, thermal diffusion presents the primary obstacle to multilayer integration by accelerating evaporation of liquid volumes in the controlled fluidic network due to inter-layer heat transfer. Along with our suggested geometric modifications, a different choice of substrate materials would also likely help to suppress undesired heat transfer. For example, replacement of our Si/glass stack with a glass/PDMS stack (k_{Si} = 148 W m^{-1} K^{-1}; k_{glass} = 1.2 W m^{-1} K^{-1}; k_{PDMS} = 0.15 W m^{-1} K^{-1}) would greatly reduce the overall thermal conductivity of the device, simultaneously decreasing power consumption and thermal diffusion. Addressing these issues will greatly increase the viability and versatility of the Venturi microregulator array as a universal microfluidic flow control platform.

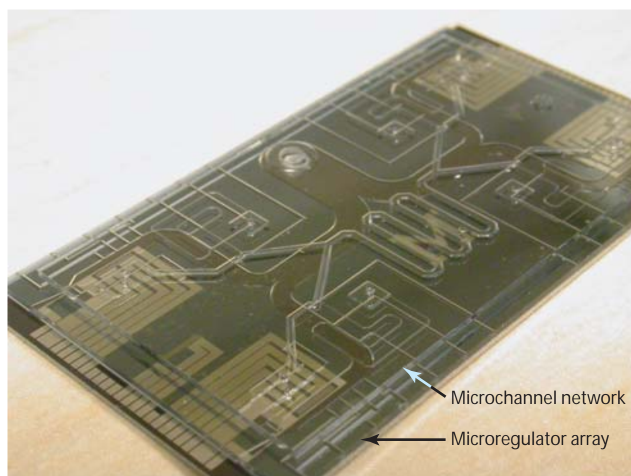

Figure 3.11: Three-layer device integrating Venturi microregulator array and microfluidic network.

References

[1] R. Khnouf, D. J. Beebe and Z. H. Fan, Cell-free protein expression in a microchannel array with passive pumping, *Lab Chip*, 2009, **9**, 56-61.
[2] S. Cesaro-Tadic, G. Dernick, D. Juncker, G. Buurman, H. Kropshofer, B. Michel, C. Fattinger and E. Delamarche, High-sensitivity miniaturized immunoassays for tumor necrosis factor α using microfluidic systems, *Lab Chip*, 2004, **4**, 563-569.
[3] Z. R. Xu, C. H. Zhong, Y. X. Guan, X. W. Chen, J. H. Wang and Z. L. Fang, A microfluidic flow injection system for DNA assay with fluids driven by an on-chip integrated pump based on capillary and evaporation effects, *Lab Chip*, 2008, **8**, 1658-1663.
[4] K. H. Chung, J. W. Hong, D. S. Lee and H. C. Yoon, Microfluidic chip accomplishing self-fluid replacement using only capillary force and its bioanalytical application, *Anal Chim Acta*, 2007, **585**, 1-10.
[5] J. Melin, N. Roxhed, G. Gimenez, P. Griss, W. van der Wijngaart and G. Stemme, A liquid-triggered liquid microvalve for on-chip flow control, *Sens Acuators B*, 2004, **100**, 463-468.
[6] M. Gustafsson, D. Hirschberg, C. Palmberg, H. Jörnvall and T. Bergman, Integrated sample preparation and MALDI mass spectrometry on a microfluidic compact disk, *Anal Chem*, 2004, **76**, 345-350.
[7] J. Steigert, M. Grumann, T. Brenner, L. Riegger, J. Harter, R. Zengerle and J. Ducrée, Fully integrated whole blood testing by real-time absorption measurement on a centrifugal platform, *Lab Chip*, 2006, **6**, 1040-1044.
[8] Y. K. Cho, J. G. Lee, J. M. Park, B. S. Lee, Y. Lee and C. Ko, One-step pathogen specific DNA extraction from whole blood on a centrifugal microfluidic device, *Lab Chip*, 2007, **7**, 565-573.
[9] S. Lai, S. Wang, J. Luo, L. J. Lee, S. T. Yang and M. J. Madou, Design of a compact disk-like microfluidic platform for enzyme-linked immunosorbent assay, *Anal Chem*, 2004, **76**, 1832-1837.
[10] F. Amirouche, Y. Zhou and T. Johnson, Current micropump technologies and their biomedical applications, *Microsyst Technol*, 2009, **15**, 647-666.
[11] K. W. Oh and C. H. Ahn, A review of microvalves, *J Micromech Microeng*, 2006, **16**, R13-R39.
[12] C. Zhang, D. Xing and Y. Li, Micropumps, microvalves, and micromixers within PCR microfluidic chips: Advances and trends, *Biotech Adv*, 2007, **25**, 483-514.
[13] M. A. Unger, H. P. Chou, T. Thorsen, A. Scherer and S. R. Quake, Monolithic microfabricated valves and pumps by multilayer soft lithography, *Science*, 2000, **288**, 113-116.
[14] D. S. Chang, S. M. Langelier and M. A. Burns, An electronic Venturi-based pressure microregulator, *Lab Chip*, 2007, **7**, 1791-1799.
[15] C. H. Lee, K. Jiang and G. J. Davies, Sidewall roughness characterization and comparison between silicon and SU-8 microcomponents, *Materials Characterization*, 2007, **58**, 603-609.
[16] M. Yang, R. Pal and M. A. Burns, Cost-effective thermal isolation techniques for use on microfabricated DNA amplification and analysis devices, *J Micromech Microeng*, 2005, **15**, 221-230.
[17] N. Srivastava and M. A. Burns, Electronic drop sensing in microfluidic devices: Automated operation of a nanoliter viscometer, *Lab Chip*, 2006, **6**, 744-751.
[18] M. C. Cole and P. J. A. Kenis, Multiplexed electrical sensor arrays in microfluidic networks, *Sens Actuators B*, 2009, **136**, 350-358.

CHAPTER 4

Viscous Effects in Low Re Planar Micronozzles

Introduction

Microscale nozzles have generated interest for a variety of applications. Unsurprisingly, the majority of these applications relate to propulsion due to the favorable thrust to weight ratio of these structures. Orbital maneuvering and attitude adjustment microthrusters for micro- and nanosatellites are particularly appropriate given the low mass of the intended spacecraft (~ 1 – 10 kg). Although macroscale nozzles are generally well characterized by inviscid flow theory, significant deviations arise with decreasing length scale because of the increasing importance of viscous energy dissipation. The need for accurate prediction of the thrust produced by microthrusters has thus resulted in considerable effort being expended on modeling size effects on nozzle performance.

Research efforts characterizing micronozzle performance have predominantly focused on axisymmetric and two-dimensional geometries. Computational analyses of conical micronozzles have provided detailed models of both steady and unsteady state thrust based on nozzle geometry.[1,2] More commonly, experimental studies have employed nozzles of rectangular cross-section in which the height (the dimension orthogonal to the plane containing the area change) is much larger than the throat width,

such that the flow behavior can be acceptably approximated by 2D computational analyses.[3,4,5,6,7] Fabrication methods for these micronozzle test geometries include milling of metals and deep reactive ion etching of silicon, producing throat widths ranging from upwards of several millimeters down to 20 μm. A decrease in Reynolds number (*Re*) accompanies the decrease in the characteristic length scale, offering one way to quantify the corresponding increase in viscous energy dissipation. The major result of this size scaling is decreased Mach number (*M*)—and thus reduced thrust—at the exit plane relative to the inviscid case due to the development of thick boundary layers that can occupy the full cross section of the nozzle outlet. Gas flows at very small length scales on the order of 1 μm have been used to study rarefaction effects at high Knudsen numbers ($Kn > 0.01$) where continuum mechanics break down.[8]

More recently, researchers have investigated many novel microfabricated geometries to exploit gas dynamics for microfluidic flow control. Li *et al.*[9] and Mishra and Peles[10,11] published detailed studies of both liquid and gas flows through microorifices. Flow control systems employing Venturi pumps[12,13] and recursive channel networks[14] to produce differential pressures in microfluidic devices have been developed by various groups. Cho *et al.*[15] and Morimoto *et al.*[16] developed fluidic amplifiers and oscillators based on mechanical perturbation of jetting flows. Diverse applications including microthrusters[17], fluidic diodes[18], and gas concentrators[19] have utilized rounded geometries capable of generating vortices and centripetally accelerated flows. The reliance on inertially dominated phenomena for the intended operation of all these systems demands a fundamental understanding of viscous scaling effects for optimized design of their respective flow geometries.

Our group has explored the use of thermally perturbed micronozzle gas flows for distributed pressure control in lab-on-a-chip platforms.[20] The core component of these controllers is a micronozzle operating as a Venturi with the output pressure of the controller provided through a sidearm that taps into the nozzle throat. Sufficiently high inlet pressures produce negative throat pressures and thus a negative output pressure at room temperature. Upon heating, the throat pressure, and correspondingly the output pressure, become positive. The low mass flow through the micronozzle limits the maximum flow rate through the sidearm, thereby allowing coordinated controllers to precisely manipulate microliter liquid volumes coupled to the sidearm. Additionally, the high rate of heat transfer into the flow enabled by the large surface area to volume ratio of the structure produces a fast response time. Like the applications mentioned already, proper scaling of the micronozzle geometry in the controller is critical to ensure that viscous energy dissipation is sufficiently low to permit generation of negative throat pressures yet sufficiently high as to maximize the changes in the flow field effected by heating.

In our current work, we characterize the impact of viscous effects in planar micronozzles (throat width exceeds nozzle height) in the transitional *Re* regime ($Re \sim 10^2 - 10^3$) to better elucidate the flow behavior of our previously introduced Venturi microregulator pressure controller. Martinelli and Viktorov observed that increasing aspect ratio increases the entrance length of rectangular microchannel flows.[21] It thus stands to reason that boundary layer development in planar micronozzles should also differ from 2D and axisymmetric nozzles. Given the design of the Venturi microregulator, our study concentrates on the converging portion of the nozzle geometry

upstream of the throat. Previous studies of similar geometries employed throat hydraulic diameters greater than 200 µm operated at high *Re* on the order of 10,000.[22] Combining experimental and computational data, we aim to provide qualitative understanding of boundary layer structure and viscous effects in low *Re* planar micronozzles.

Materials and Methods

Micronozzle design and fabrication

Micronozzles, photolithographically defined using the mask shown in Fig. 4.1a, were fabricated in glass. Chromium and gold (500/3500 Å) were evaporated on Borofloat glass wafers (700 µm thick, 10 cm diameter) cleaned in piranha solution (H_2SO_4/H_2O_2, 3:1). Photoresist (Microposit SC 1827; Shipley Co., Marlborough, MA) was spun on, exposed, and developed using standard photolithography techniques. The developed wafer was hard baked at 140°C for 15 min. The gold was etched for 2 min (gold etchant TFA; Transene Co., Danvers, MA), and the chromium was etched for 2 min (chromium etchant CR-14; Cynatek Corp., Fremont, CA), masking the glass wafer with the patterned metal. The exposed glass was isotropically etched in hydrofluoric acid (49% HF, CMOS grade; J.T. Baker, Philipsburg, NJ) to depths of 24 µm, 48 µm, 72 µm, 80 µm, 93 µm, and 151 µm. Because the same photomask was used for all etch depths, the area ratios of the resulting geometries varied as detailed in Table 4.1. After dicing to separate the individual devices, air inlet holes were drilled using a high-speed drill press with a diamond-tipped bit (1.5 mm diameter; UKAM Industrial Superhard Tools, Valencia,

CA). Sidearm access holes of 0.5 mm diameter were drilled by electrochemical discharge machining.

Table 4.1: Area Ratios of Fabricated Micronozzles

Etch Depth, Micronozzle Height (μm)	Fabricated Area Ratio (A_{in}/A_{throat})
24	10.8
48	9.7
72	8.8
80	7.8
93	8.8
151	6.5

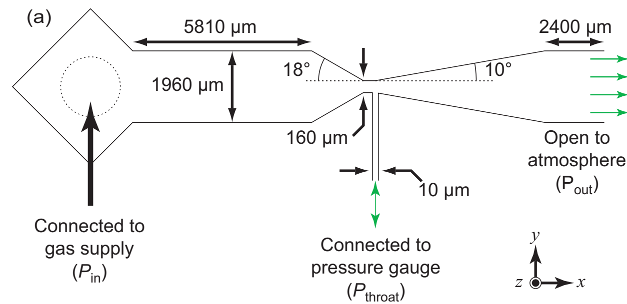

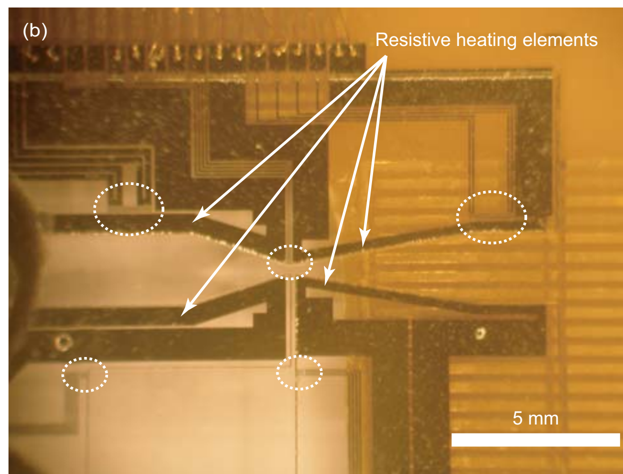

Figure 4.1: Experimental micronozzle structure. (*a*) Diagram showing geometric parameters of photomask used to fabricate micronozzles. (*b*) Image of nozzle portion of assembled Venturi microregulator. The five temperature sensors in this design are circled.

The diced devices were cleaned with acetone, isopropyl alcohol, and de-ionized water. The cleaned devices were bonded against glass microscope slides using UV curable optical glue (NOA 72; Norland Products, Cranbury, NJ) applied at the edge of the device and allowed to wick in between the glass surfaces by capillary action. The glue was cured according to the manufacturer's instructions. Syringe tips (Part Number 5114-B-90; EFD Inc., East Providence, RI) glued to glass routing posts (2 mm I.D.) were attached to the fluid inlets with epoxy (Steel Weld Epoxy; ITW Performance Polymers, Riviera Beach, FL) for interfacing with off-chip connections.

Micronozzles used for thermal experiments were assembled as Venturi microregulators, pictured in Fig. 4.1b and 4.1c. In lieu of bare microscope slides, the lower glass substrate was patterned with heating elements and four-point resistive temperature detectors (RTD). To fabricate these electronic components, bare Borofloat wafers cleaned in piranha solution were lithographically processed as in the nozzle fabrication procedure to generate a liftoff mask outlining the desired metal lines but were not hard baked. Titanium and platinum (300/1000 Å) were evaporated onto the developed wafer. The wafer was sonicated in acetone (CMOS grade; J.T. Baker) for 10 min to remove unwanted metal. The measured resistances of the heaters and RTDs were approximately 40 Ω and between 500 and 2000 Ω, respectively. The wafer was diced to obtain the individual devices.

Micronozzle operation and characterization

Pressurized air, helium, or argon was continuously fed through a mass flow controller (1100 Series; MKS Instruments, Inc., Andover, MA) to the micronozzle inlet. For thermal perturbation experiments, gas supplies were instead controlled by a pressure regulator (Model Number 3476A; Matheson Gas Products Inc, Irving, TX), and mass flow was measured just upstream of the micronozzle inlet using an inline hotwire anemometer. All pressure measurements at the throat were taken using an electronic pressure sensor (Strain Gage Panel Meter DP25B-S; Omega, Stamford, CT). All pressure and temperature measurements were recorded after equilibrating to their steady-state values.

For thermal perturbation experiments, the microfabricated heaters and RTDs were controlled by a DC power supply (Model Number HY5003; Mastech, Hong Kong), two data acquisition (DAQ) boards (PCI-6031E and PCI-6704; National Instruments, Austin, TX), two connector blocks (SCB-100 and SCB-68; National Instruments), a custom signal conditioning circuit, a computer, and a LabVIEW program (National Instruments).

Micronozzle simulation

Three-dimensional numerical simulations of micronozzle flow were performed using the commercial computational fluid dynamics package FLUENT. Geometries possessing length, converging/diverging angle, and area ratio identical to our fabricated micronozzles were modeled with two planes of symmetry, one parallel to the *xy*-plane and one parallel to the *xz*-plane. This mirroring results in inaccurate modeling of specific flow patterns in the diverging section of the nozzle, particularly downstream of boundary layer separation and standing shocks, and prevents solution convergence at very high inlet pressures. However, the simulated flow upstream of the throat and overall mass flow rate, the main interests of this study, are negligibly affected.

The simulation geometries were meshed with 126 nodes in the *x*-dimension, 31 nodes in the *y*-dimension, and 21 nodes in the *z*-dimension with finer meshing towards the walls to better resolve boundary layer structure. All walls were fixed with no-slip, isothermal boundary conditions; wall temperatures were uniformly changed for thermal perturbation simulations. A constant pressure boundary condition was applied at the nozzle inlet with the inlet temperature always set equal to the wall temperature. The nozzle outlet was fixed at 101 kPa and 293 K. The k-ε turbulence viscous model was used in all cases with the default setting of 10 percent turbulent intensity. Neither lower turbulent intensity values nor use of the laminar viscous model produced significant changes in the solutions. Fluid density was calculated as an ideal gas, and fluid viscosity was modeled using the Sutherland equation. Simulations were considered converged when all residuals decreased below 10^{-3}.

Results and Discussion

Reynolds number dependence of micronozzle behavior

The characteristic length scale, represented by the *z*-dimensional height (H), of planar micronozzle geometries primarily determines the relative significance of viscous effects on the interior flow. The Reynolds number

$$\mathrm{Re} \equiv \frac{\rho U H}{\mu} = G \cdot \frac{H}{\mu}, \tag{4.1}$$

defined as a ratio of inertial forces ($\sim \rho U^2$) to viscous forces ($\sim \mu U/H$), quantifies this significance with respect to flow geometry, fluid velocity (U), and kinematic viscosity ($\nu = \mu/\rho$). As shown in Eqn. 4.1, *Re* can also be expressed in terms of the mass flux (G) by substituting $G = \rho U$ from the continuity equation. The reciprocal of *Re* emerges as the scaling coefficient accompanying the shear component of the stress tensor upon proper non-dimensionalization of the Navier-Stokes equations. Small *Re* therefore indicate that momentum transfer is mainly diffusive as opposed to convective and vice versa for large *Re*. Because nozzles function to convert pressure energy into kinetic energy, *Re* provides some insight into the efficiency of a given nozzle with small *Re* being indicative of large diffusive momentum losses into the boundary layer.

Figure 4.2a depicts the influence of the characteristic length scale on mass flux at the throat as the axial pressure gradient down the micronozzle is increased. Intuitively, a lower fluid velocity is expected in the viscous dominated region of the flow near the stationary nozzle walls. For small nozzle heights, this viscous region occupies a greater proportion of the cross-sectional area, resulting in a lower mass flux relative to larger nozzles. The high aspect ratio, rectangular slit cross-section inherent to our planar

microfabricated geometry causes the largest velocity gradients to be in the *xz*-plane. Subsequently, the nozzle height overwhelmingly dictates the viscous energy dissipation, in a manner conceptually similar to Hele-Shaw flow. On the other hand, the area ratio of the nozzle is exclusively determined in the *xy*-plane, allowing inertial effects to be decoupled from viscous effects during design of the flow geometry.

The dependence of mass flux on inlet pressure can be divided into two flow regimes, distinguished by the distinct change in slope in each curve of Fig. 4.2a. At low inlet pressures, compressibility effects are negligible; therefore mass flux, which is the product of fluid density and fluid velocity, varies primarily according to the flow velocity. For nozzles of small hydraulic diameter, flow is laminar, so flow velocity increases linearly with pressure. For large hydraulic diameters, inertial forces dominate such that flow velocity increases with the square root of pressure. In this first flow regime, the rate at which mass flux increases with inlet pressure varies inversely with the hydraulic resistance of the nozzle. In the second regime, the dependence of mass flux on inlet pressure becomes identical irrespective of nozzle geometry as shown by the identical slope among all curves. The flow is choked such that velocity no longer increases with increasing inlet pressure; instead, changes in mass flux are solely attributable to changing fluid density.

This observation demonstrates that any given nozzle geometry can operate across multiple flow regimes depending on the magnitude of the imposed axial pressure gradient. Figure 4.2b identifies these operating regimes for a single geometry. At low inlet pressures (P_{in}), the throat pressure (P_{throat}) exceeds the outlet pressure. In this low *Re* regime, the laminar flow is dominated by viscous momentum transfer, and the axial

pressure distribution monotonically decreases between the inlet and outlet of the micronozzle. As P_{in} increases, Re grows until the flow eventually becomes inertially dominated. In the intermediate Re regime, the relative contribution of inertial forces exceeds that of the viscous forces. The throat pressure is negative and decreases monotonically with increasing P_{in} in accordance with Bernoulli's principle. Under these conditions, the flow is subsonic, and the nozzle operates as a Venturi. At the inlet pressure corresponding to the minimum constriction pressure, $M = 1$ at the throat. Further increase of P_{in} causes the flow to choke and P_{throat} to rise. Although higher inlet pressures negligibly change the fluid velocity, higher Re values are still attained due to decreasing kinematic viscosity.

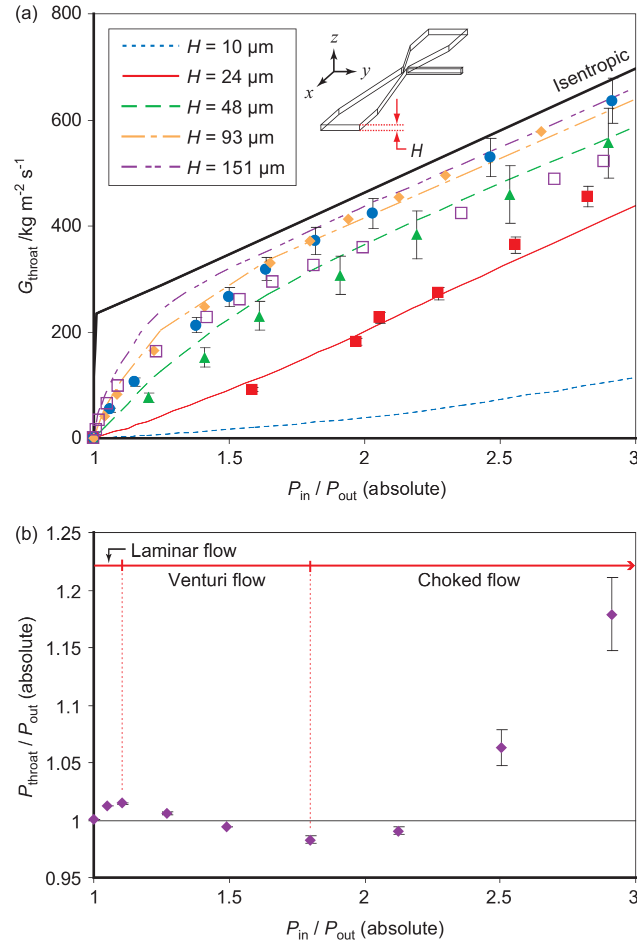

Figure 4.2: Flow characteristics of experimental micronozzles. (*a*) Variation of mass flux at the throat with inlet pressure at different characteristic length scales. Points represent experimental data (■ H = 24 μm; ▲ H = 48 μm; ● H = 72 μm; ♦ H = 93 μm; □ H = 151 μm) while lines represent simulation results. Note that the concavity of the curves changes from negative to positive between H = 24 μm and H = 48 μm. The deviation from expected behavior for H = 151 μm may be due to excessive wall roughness resulting from the prolonged glass etch during fabrication, which should increase frictional momentum losses. (*b*) Experimental characterization of micronozzle operating regimes at low *Re* (H = 80 μm; P_{out} = 101 kPa). Error bars indicate one standard deviation above and below the mean of triplicate measurements based on known sources of error.

Viscous wall effects

The significance of viscous wall effects is best shown by examination of the fluid velocity profile along the centerline and normal to the wall in the z-direction. To this end, simulation of our experimental micronozzle geometries is particularly useful given the challenge of empirically acquiring such measurements in gas-phase microscale systems. Figure 4.3 compares the simulated centerline velocity profiles along the z-dimension at the throat of several micronozzles operated in the laminar regime ($Re \approx 275$) and in the choked flow regime ($Re \approx 2500$). At low Re, the viscous-dominated, boundary layer—defined as the contiguous region extending from the stationary wall in which the fluid velocity does not exceed 99 percent of the centerline velocity—occupies a similar fraction of the flow cross-section for all nozzle heights. At high Re, a flat inertially dominated core region, where the maximum fluid velocity is capped by the sonic limit ($M = 1$), that is distinct from the parabolic boundary layer region becomes distinguishable.

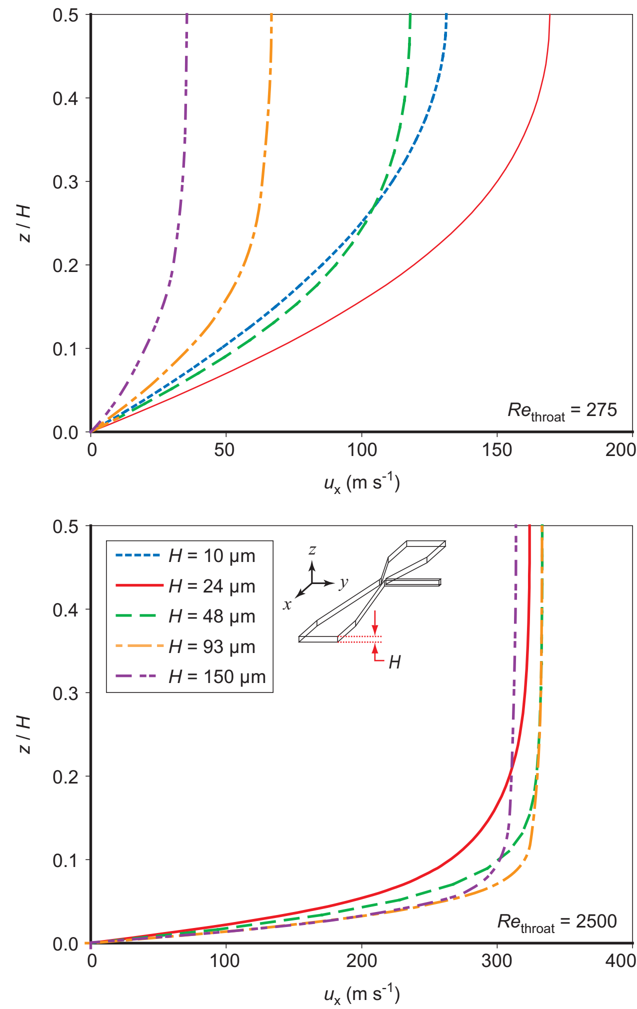

Figure 4.3: Simulated throat velocity distributions. Axial velocity (u_x) is plotted against the z-position normalized by the nozzle height for Re_{throat} = 275 (*top*) and Re_{throat} = 2500 (*bottom*) where z = 0 corresponds to the wall and z = 0.5H corresponds to the centerline. No result is shown for H = 10 µm at Re_{throat} = 2500 due to the inability to find a convergent solution.

The fraction of the flow occupied by the boundary layer also varies greatly with increasing flow rate. As shown in Fig. 4.4a, the boundary layer thickness (ζ) is significantly reduced by increases in *Re* for large nozzle heights; however, ζ for small nozzle heights remains mostly insensitive to these changes because the core region has already reached $M = 1$ at relatively low *Re*. Due to the difficulty of experimentally measuring gas velocity at the throat, we substitute the alternative parameter ξ in place of the Mach number as a qualitative indicator of proximity to the choked condition. We define ξ as the mass flux at the throat divided by the isentropic mass flux when $M = 1$ at the throat of the same geometry. Figure 4.4b shows that the boundary layer thickness decreases drastically for large nozzle heights as the flow chokes, whereas the change in boundary layer thickness is negligible for very small nozzle heights. The calculated displacement thickness (δ) and momentum thickness (θ) evolve similarly (data not shown), where δ and θ are defined as

.

$$\delta \equiv \int_0^{H/2} \left(1 - \frac{\rho u}{\rho_0 u_0}\right) dz \approx \frac{\zeta}{4} \tag{4.2}$$

$$\theta \equiv \int_0^{H/2} \left(1 - \frac{u}{u_0}\right) \frac{\rho u}{\rho_0 u_0} dz \approx \frac{\delta}{3} \tag{4.3}$$

and ρ_0 and u_0 are the centerline density and velocity.

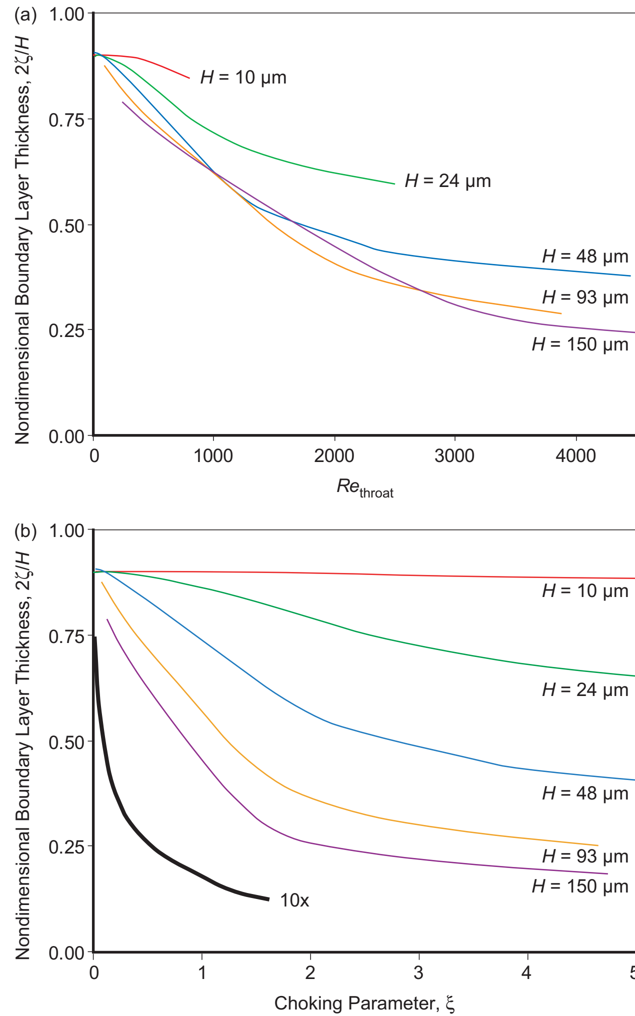

Figure 4.4: Simulated boundary layer development with Re_{throat}. The boundary layer thickness (ζ) is defined as the distance from the wall where the fluid velocity first reaches 99 percent of the centerline velocity. (*a*) The fraction of the total channel height occupied by both boundary layers at the throat is plotted against Re_{throat}. (*b*) The fraction of the total channel height occupied by both boundary layers at the throat is plotted against the choking parameter ξ, defined as the throat mass flux divided by the corresponding isentropic mass flux at the onset of choking. The data series labeled "10x" was simulated using the 150 μm geometry scaled ten times in all linear dimensions (H = 1.5 mm). Observe that the boundary layer thickness becomes increasingly insensitive to flow rate at smaller length scales.

A more experimentally accessible strategy for characterizing the impact of viscous wall effects is analyzing mass flux (*G*). Because the inlet pressure affects mass flow through both changes in density and changes in velocity when the flow is not choked, it is useful to nondimensionalize the mass flux with respect to the stagnation conditions. From the continuity equation

$$G = \rho u \, , \tag{4.4}$$

1D isentropic flow relationships for a perfect gas,

$$\rho = \rho_t \left(1 + \frac{\gamma - 1}{2} M^2\right)^{\frac{-1}{\gamma - 1}} \tag{4.5}$$

$$T = T_t \left(1 + \frac{\gamma - 1}{2} M^2\right) \tag{4.6}$$

$$M \equiv \frac{u}{a} = \frac{u}{\sqrt{\gamma \Re T}} \tag{4.7}$$

and the ideal gas law relating the stagnation conditions

$$\rho_t = \frac{P_t}{\Re T_t} \, ,$$

we can derive

$$G = M \cdot \left(1 + \frac{\gamma - 1}{2} M^2\right)^{\frac{-(\gamma+1)}{2(\gamma-1)}} \cdot P_t \sqrt{\frac{\gamma}{\Re T_t}} \, . \tag{4.8}$$

Defining ψ to be the nondimensional mass flux

$$\begin{aligned} \psi &\equiv G \cdot \left(P_t \sqrt{\frac{\gamma}{\Re T_t}}\right)^{-1} = M \cdot \left(1 + \frac{\gamma - 1}{2} M^2\right)^{\frac{-(\gamma+1)}{2(\gamma-1)}} \\ &\approx G \cdot \left(P_{in} \sqrt{\frac{\gamma}{\Re T_{in}}}\right)^{-1} \end{aligned} \, , \tag{4.9}$$

we see that ψ reaches a limiting value of 0.579 at the throat for air when the flow chokes and $M = 1$.

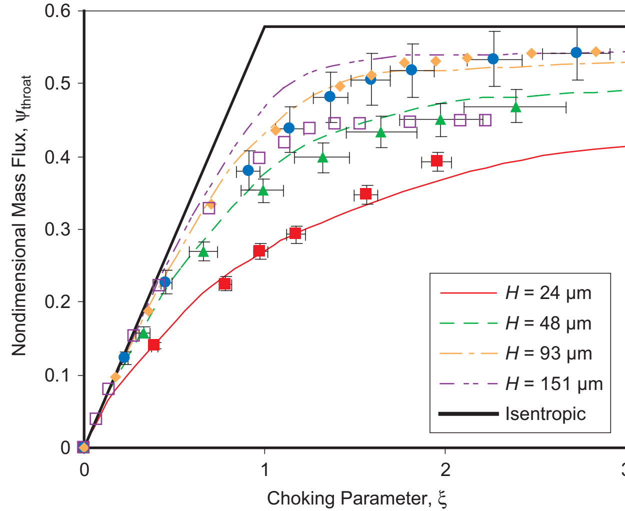

Figure 4.5: Deviation of viscous micronozzle performance from isentropic flow. The nondimensional mass flux at the throat ψ_{throat} (Eqn. 4.9) is plotted against the choking parameter ξ, defined as the throat mass flux divided by the corresponding isentropic mass flux at the onset of choking. Points represent experimental data (■ $H = 24$ μm; ▲ $H = 48$ μm; ● $H = 72$ μm; ♦ $H = 93$ μm; □ $H = 151$ μm). Note that viscous energy dissipation is proportionally greater for smaller values of H, resulting in larger deviation from the isentropic case and a slower asymptotic increase towards choked flow. Error bars indicate one standard deviation above and below the mean of triplicate measurements based on known sources of error.

We plot ψ at the throat against the choking parameter (ξ) for different micronozzles in Fig. 4.5. The increasing importance of viscous energy dissipation with decreasing nozzle height is apparent in the growing deviation from the inviscid case. The asymptotic increase of ψ_{throat} shifts to higher values of ξ as nozzle height decreases, or equivalently, the onset of choking occurs at higher inlet pressures. Simulations of micronozzles possessing different area ratios but the same height fall along a single curve as shown in Fig. 4.6a, suggesting that the large aspect ratio of our geometry does suppress edge effects to reasonably allow decoupling of the *z*-dimension from the nozzle contour in the *xy*-plane.

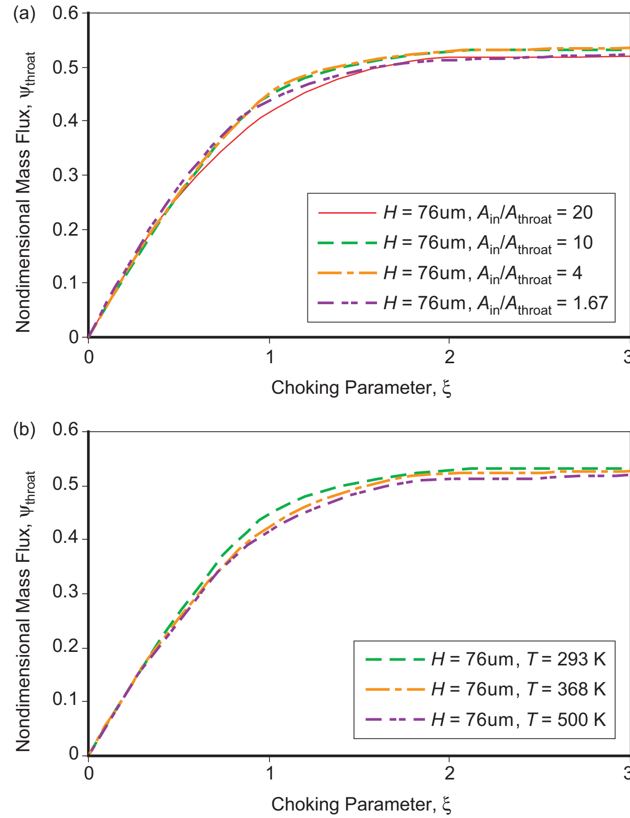

Figure 4.6: Simulated mass flow in micronozzles with varying area ratio and heat addition. (*a*) Simulation results for nozzles of equal height but unequal area ratios (T = 293 K) fall along a single curve. (*b*) Simulation results for nozzles of equal height but different wall temperatures (area ratio, A_{in}/A_{throat} = 10) show a slightly increasing deviation from the isentropic case with increasing heat addition, most likely due to the nonuniform heat flux along the length of the nozzle.

In our previous work, we attributed observed decreases in mass flow rate and increases in throat pressure in response to increasing temperature to increased gas viscosity; this phenomenon formed the operational basis of the Venturi microregulator. A temperature increase of 75 degrees from 293 K to 368 K produces a 15 percent increase in the viscosity of air. According to simulation data, this temperature change at the wall increases the velocity boundary layer thickness by approximately 5 percent of the nozzle height as shown in Fig. 4.7. Because heat addition occurs through the nozzle wall in the simulation and experimental systems, a thermal boundary layer also exists. The thickness

of the thermal boundary layer exceeds the thickness of the velocity boundary layer (Pr = 0.7); the overall mass flux and convective momentum flux thus do not decrease significantly as a result of the viscosity increase because the density—and subsequently, the mass flux—in the viscous wall region is less than the density in the inertial core (Fig. 4.8b). This effect is clearly shown by the negligible increase in momentum thickness (Eqn. 3) and displacement thickness (Eqn. 2) with heating (Fig. 4.7). However, the increased centerline velocity combined with the increased fluid viscosity does result in a 17 percent rise in the wall shear stress, which increases momentum transfer out of the flow and decreases the difference between the throat pressure and the fixed inlet pressure. This increase in shear stress accounts for the precise pressure control capability of the Venturi microregulator because the momentum flux into the wall equates to only 3.7 percent of the convective momentum flux.

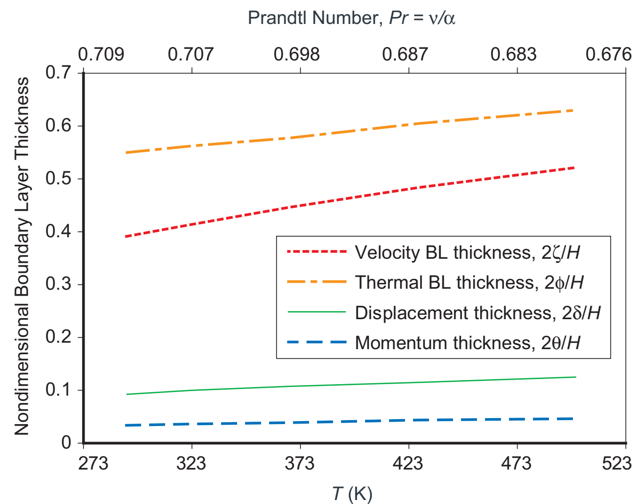

Figure 4.7: Simulated boundary layer thickness with heat addition for $H = 80$ µm. The velocity and themal boundary layer thicknesses, displacement thickness, and momentum thickness nondimensionalized by the nozzle half-height are plotted as a function of wall temperature and Prandtl number. Note the negligible change in momentum thickness despite the substantial increase in boundary layer thickness.

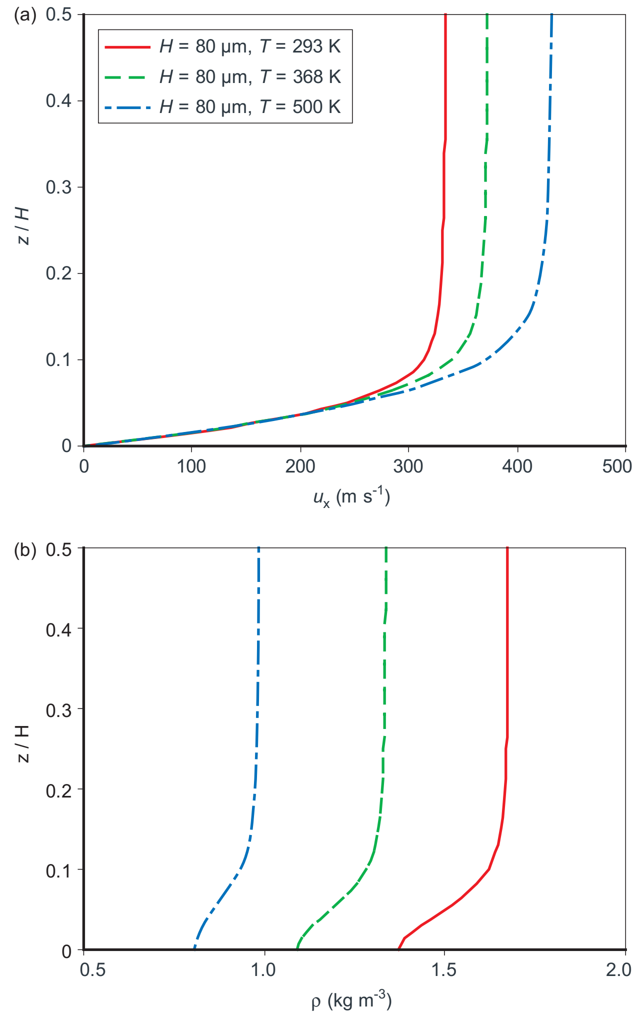

Figure 4.8: Simulated velocity and density profiles with heat addition for $H = 80$ μm. (*a*) Axial velocity (u_x) is plotted against the normalized *z*-position at the nozzle throat. Observe that the centerline velocity increases with wall temperature due to the rise in sonic velocity. (*b*) Density (ρ) is plotted against the normalized *z*-position at the nozzle throat. The gas density increases with increasing distance from the heated wall, providing an indication of the thermal boundary layer thickness.

Figure 4.9 shows that the normalized change in mass flow rate measured in our simulated system closely matches the decrease predicted by inviscid Rayleigh flow despite the sizeable fraction of the flow dominated by viscous momentum transfer. In the inviscid case, the fluid velocity profile is assumed not to vary according to distance from the walls, and heat addition uniformly increases the fluid velocity at all positions along the axial dimension. Although the corresponding velocity profile for a real fluid is nonuniform due to viscous effects, the agreement in the normalized change in mass flux between the inviscid and simulated systems suggests that the primary changes in mass and momentum flux occur in the inertially dominated core. In other words, changes in mass and momentum flux that occur in the viscous-dominated wall region contribute much less significantly to changes in the overall flow rate. This corroborates our previous observation of negligible change in the displacement and momentum thicknesses with heat addition.

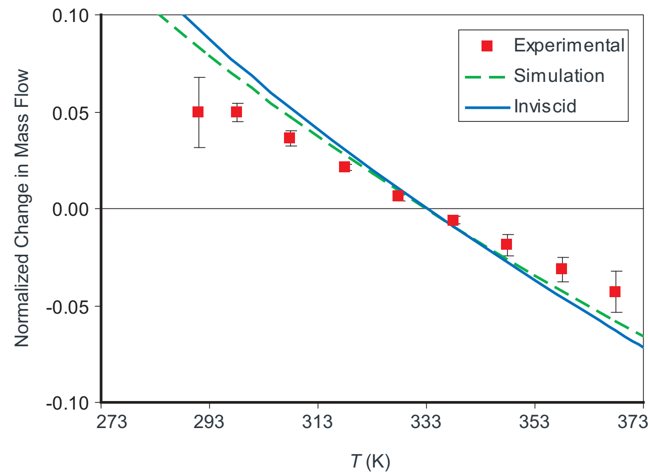

Figure 4.9: Changes in mass flow with heat addition in experimental micronozzles. Changes in mass flow are normalized to the mass flow rate at $T = 333$ K and plotted against the wall temperature (T). The observed deviation between experimental and simulation results is due to nonideal heat transfer in the experimental system, causing the wall temperature to be greater than the actual temperature of the fluid. Error bars indicate one standard deviation above and below the mean of triplicate measurements.

Other gases

Micronozzle performance also varies according to the composition of the gas flow. Diatomic nitrogen constitutes 78 percent of air by volume. Monatomic gases such as helium and argon should exhibit a greater response to thermal perturbation because of their higher specific heat ratio (γ) and lower heat capacity (C_p). In the context of the Venturi microregulator, simple scaling analysis predicts a 10 percent increase in the output pressure range with the substitution of argon for air as the working fluid, primarily resulting from the increase in sonic velocity.

Table 4.2: Gas Properties at 20 °C, 1 atm

Gas	γ	MW (g mol^{-1})	C_p (J mol^{-1} K^{-1})	k (W m^{-1} K^{-1})	μ (Pa s^{-1})	$\nu \equiv \mu/\rho$ (m^2 s^{-1})
Air	≈ 1.4	29	29.0	0.024	1.8×10^{-5}	1.4×10^{-5}
He	1.66	4	20.8	0.142	1.9×10^{-5}	1.1×10^{-4}
Ar	1.66	40	20.8	0.016	2.2×10^{-5}	1.2×10^{-5}

At the microscale, the most important difference between helium and the other two gases is kinematic viscosity. This sharp disparity results from the unequal density of these fluids. Flows of similar velocity in the same micronozzle geometry will be characterized by smaller *Re* for helium than for air or argon. Physically, this manifests as proportionally greater viscous energy dissipation, exemplified by the inability to produce negative throat pressures in certain experimental micronozzles upon exchanging helium for air (Fig. 4.10). Figure 4.11a shows the mass flux of helium and argon with changing inlet pressure. Whereas argon behaves comparably to air, the curves for helium exhibit the positive concavity indicative of laminar flow at larger nozzle heights than for air. This greater deviation from the inviscid case due to viscous wall effects is also observed in the

nondimensional mass flux (Fig. 4.11b) where the asymptotic increase toward the choked flow limit is slower for helium than for air and argon.

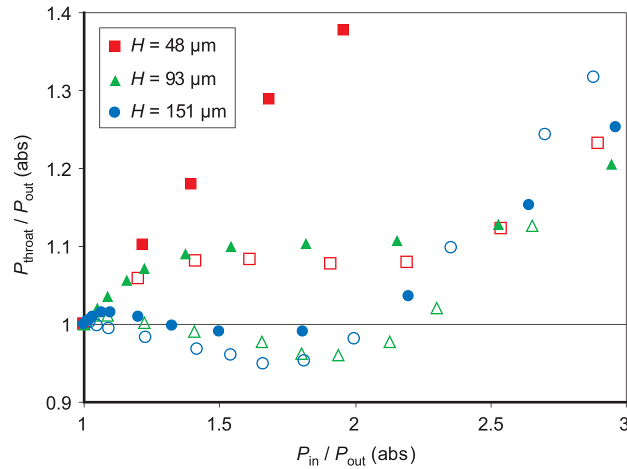

Figure 4.10: Experimental variation of throat pressure with inlet pressure for helium operated micronozzles. Nozzle geometries capable of generating negative throat pressures with air (open symbols) may not be able to generate negative pressures with helium (filled symbols) due to the ten times decrease in kinematic viscosity. Note the similarity between helium at $H = 93$ µm and air at $H = 48$ µm.

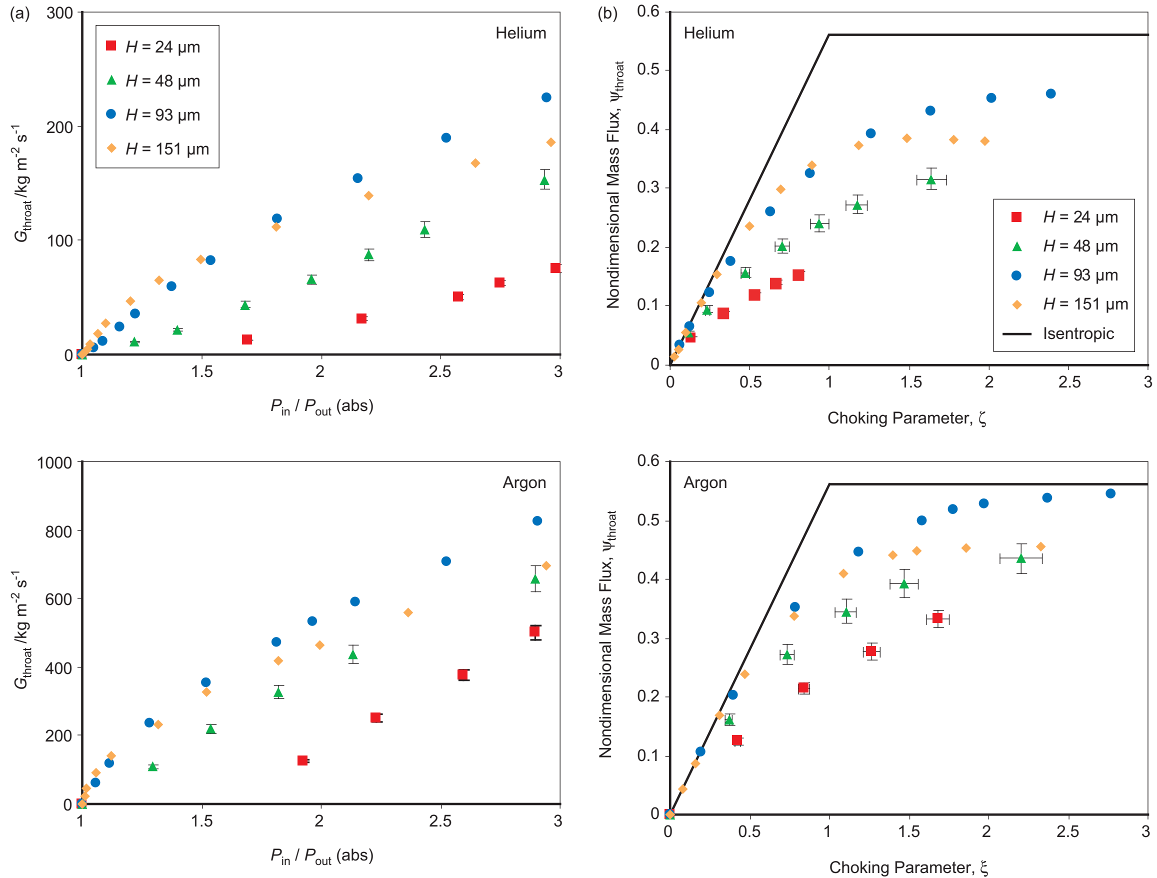

Figure 4.11: Mass flux at the throat of experimental micronozzles operated with helium (*top*) and argon (*bottom*). (*a*) Note that the concavity of the curves changes from positive to negative at larger length scales for helium than for argon, which behaves similarly to air. (*b*) Nondimensional mass flux at the throat (ψ_{throat}) is plotted against the choking parameter (ξ). Due to the lower kinematic viscosity of helium, observe that viscous energy dissipation is proportionally greater for smaller values of H, resulting in larger deviations from the isentropic case and a slower asymptotic increase towards choked flow than for argon in identical nozzle geometries. As previously mentioned, the deviation from expected behavior for H = 151 μm may be due to excessive wall roughness resulting from the extended glass etch during fabrication. Error bars indicate one standard deviation above and below the mean of triplicate measurements based on known sources of error.

Operation of the Venturi microregulator using argon as the working gas increases the output pressure range 20 percent as shown in Fig. 4.12a. Because sonic velocity varies with the square root of γ, the centerline velocity of the argon flow is approximately 9 percent greater than the same quantity for air. As the centerline velocity increases, the velocity gradient at the wall must also increase given that the nozzle dimensions are fixed. Combined with the higher dynamic viscosity of argon, the magnitude of the change in wall shear stress upon heating, and subsequently, the increase in throat pressure exceed those of air. Figure 4.12b shows good agreement between experimental measurements and inviscid predictions of mass flow, consistent with the behavior previously observed for air even despite the significantly lower *Re* of the helium flow.

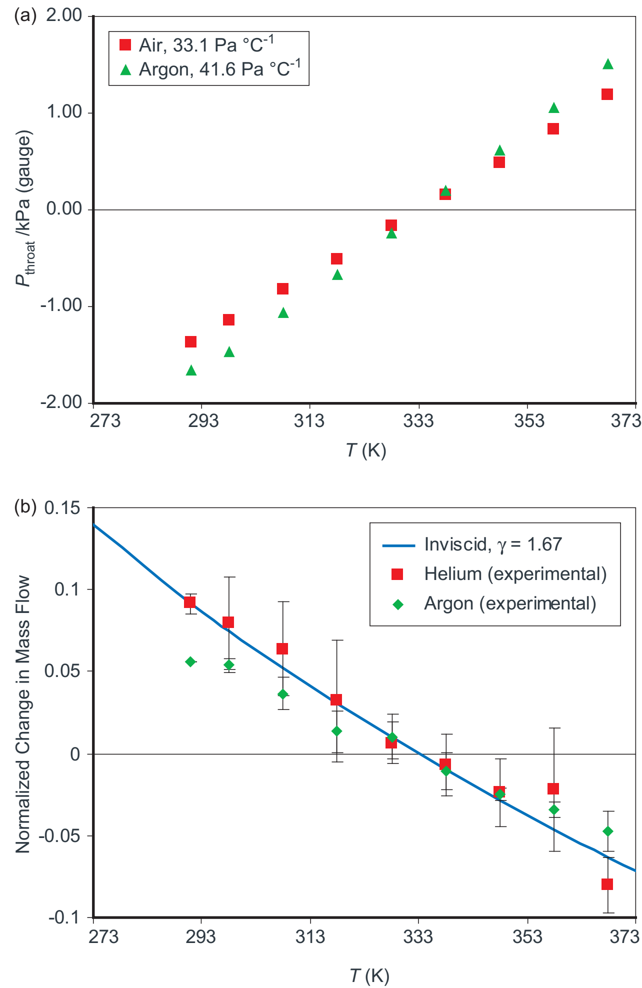

Figure 4.12: Changes in throat pressure and mass flow with heat addition in experimental helium and argon micronozzles. Experimental and simulation data are plotted against the wall temperature (T). (a) Experimental operation of the Venturi microregulator ($H = 80$ µm) substituting Ar for air as the working gas results in a 20 percent improvement in the control range due to the higher specific heat ratio, and subsequently high sonic velocity, of Ar. (b) Changes in mass flow rate are normalized to the mass flow rate at $T = 333$ K for Ar and He. The observed deviation between the experimental and simulation results is due to nonideal heat transfer in the experimental system. The deviation is smaller for He than for Ar and air because of its significantly higher thermal conductivity. Error bars indicate one standard deviation above and below the mean of triplicate measurements.

Conclusions

We have characterized viscous wall effects in planar micronozzles operating in the Venturi regime up to $M = 1$ and $Re \sim 10^3$. Experimentally measured mass flow rates demonstrate that mass flux decreases with micronozzle height in agreement with intuitive expectation. Simulations of our test geometries operated at various inlet pressures indicate that this effect chiefly arises from differences in boundary layer development tied to the characteristic length scale of the flow geometry. For large hydraulic diameters, the boundary layer shrinks rapidly with increasing inlet pressure. At smaller length scales, boundary layer thickness remains relatively insensitive to increases in fluid velocity. In addition to flow velocity, heat addition also significantly affects boundary layer development. The positive dependence on temperature of both dynamic and kinematic viscosity for gases causes heating to lead to boundary layer growth. However, because the thermal boundary layer thickness exceeds the velocity boundary layer thickness in real choked flows, changes in the boundary layer make only minor contributions to determination of the overall convective mass and momentum flux.

Gas flows allow a high degree of control over the balance of convective and diffusive modes of momentum transfer, which as we have shown, is strongly determined by the size of the flow geometry. Microscale structures are uniquely suited to capitalize on this balance given their comparable dimensions to the length scale of the viscous boundary layer. Furthermore, the extremely low viscosity and relative accessibility of compressible flow and rarefaction phenomena with gases provide access to flow regimes and control mechanisms typically inaccessible to liquid microfluidics. Geometric and thermal control of boundary layer development are only two such mechanisms, and

successful design efforts in this regard will undoubtedly require further study of these interactions.

References

[1] Lin CX, Gadepalli VVV (2009) A computational study of gas flow in a De-Laval micronozzle at different throat diameters. Int J Numer Meth Fluids 59:1203-1216. doi: 10.1002/fld.1868

[2] Rossi C, Rouhani MD, Estève D (2000) Prediction of the performance of a Si-micromachined microthruster by computing the subsonic gas flow inside the thrust. Sens Actuators A 87:96-104.

[3] Alexeenko AA, Fedosov DA, Gimelshein SF, Levin DA, Collins RJ (2006) Transient heat transfer and gas flow in a MEMS-based thruster. J Microelectromech Syst 15:181-194.

[4] Bayt RL, Breuer KS (1998) Viscous effects in supersonic MEMS-fabricated micronozzles. Proceedings of the 3rd ASME Microfluids Symposium.

[5] Hao PF, Ding YT, Yao ZH, He F, Zhu KQ (2005) Size effect on gas flow in micro nozzles. J Micromech Microeng 15:2069-2073. doi: 10.1088/0960-1317/15/11/011

[6] Xie C (2007) Characteristics of micronozzle gas flows. Phys Fluids 19:037102. doi: 10.1063/1.2709707

[7] Xu J, Zhao C (2007) Two-dimensional numerical simulations of shock waves in micro convergent-divergent nozzles. Int J Heat Mass Transfer 50:2434-2438. doi: 10.1016/j.ijheatmasstransfer.2006.11.036

[8] Arkilic EB, Schmidt MA, Breuer KS (1997) Gaseous slip flow in long microchannels. J Microelectromech Syst 6:167-178.

[9] Li X, Lee WY, Wong M, Zohar Y (2000) Gas flow in constriction microdevices. Sens Actuators A 83:277-283.

[10] Mishra C, Peles Y (2005) Size scale effects on cavitating flows through microorifices entrenched in rectangular microchannels. J Microelectromech Syst 14:987-999. doi: 10.1109/JMEMS.2005.851800

[11] Mishea C, Peles Y (2005) Incompressible and compressible flows through rectangular microorifices entrenched in silicon microchannels. J Microelectromech Syst 14:1000-1012. doi: 10.1109/JMEMS.2005.851825

[12] Chung CK, Chang WJ, Kuo YF, Hsiao CL, Weng KY (2002) Pneumatically bidirectional microfluidic regulation using Venturi pumps by deep RIE and bonding technology. Microsyst Technol 8:318-322. doi: 10.1007/S00542-001-0142-X

[13] Jen CP, Lin YC, Wu WD, Wu CY, Wu GG, Chang CC (2003) Improved design and experimental demonstration of a bi-directional microfluidic driving system. Sens Actuators B 96:701-708. doi: 10.1016/S0925-4005(03)00553-7

[14] Chung YC, Jen CP, Lin YC, Wu CY, Wu TC (2003) Design of a recursively-structured valveless device for microfluidic manipulation. Lab Chip 3:168-172. doi: 10.1039/b301750h

[15] Kim TH, Cho CH, Cho DD (1998) A three-dimensionally silicon-micromachined fluidic amplifier device. J Micromech Microeng 8:7-14.

[16] Simões EW, Furlan R, Leminski REB, Gongora-Rubio MR, Pereira MT, Morimoto NI, Avilés JJS (2005) Microfluidic oscillator for gas flow control and measurement. Flow Measurement and Instrumentation 16:7-12. doi: 10.1016/j.flowmeasinst.2004.11.001

[17] Cho C, Kim J, Cho DD (1998) A large-force fluidic device micromachined in silicon. J Micromech Microeng 8:195-199.

[18] Anduze M, Colin S, Caen R, Camon H, Conedera V, Do Conto T (2001) Analysis and testing of a fluidic vortex microdiode. J Micromech Microeng 11:108-112.

[19] Li S, Day JC, Park JJ, Cadou CP, Ghodssi R (2007) A fast-response microfluidic gas concentrating device for environmental sensing. Sens Actuators A 136:69-79. doi: 10.1016/j.sna.2006.11.035

[20] Chang DS, Langelier SM, Burns MA (2007) An electronic Venturi-based pressure microregulator. Lab Chip 7:1791-1799. doi: 10.1039/b708574e

[21] Martinelli M, Viktorov V (2009) Modelling of laminar flow in the inlet section of rectangular microchannels. J Micromech Microeng 19:025013. doi: 10.1088/0960-1317/19/2/025013

[22] Chen K, Winter M, Huang RF (2005) Supersonic flow in miniature nozzles of planar configuration. J Micromech Microeng 15:1736-1744. doi: 10.1088/0960-1317/15/9/016

CHAPTER 5

CONCLUSIONS AND FUTURE WORK

Conclusions

The overall aim of this dissertation was the investigation of new concepts and development of novel components for integrated flow control in microdevices. Our research led us to evaluate the applicability of gas flows to microfluidic systems and then to identify the relevant forces responsible for their characteristic behavior at this length scale. The exploratory strategy we adopted centered around three key elements: a specific flow geometry—the converging-diverging nozzle; a specific physical property—viscosity; and a specific perturbation mechanism—heat addition. Observations of these elements combined in varying degree, advanced our fundamental understanding of microscale gas dynamics.

The first tangible result of this dissertation was the Venturi pressure microregulator. We demonstrated the ability to output both negative and positive pressures from a single positive pressure input and electronically control that output without the use of any moving parts. The mechanism of operation is unique to the microscale. Consider that the Venturi effect is inherently inertial, yet the control mechanism is inherently viscous with the very inspiration for the idea having originated from the knowledge that gas viscosity varies positively with temperature. Our proof of

concept reveals that the size constraint enforced by the geometry produces a flow that is comparably influenced by viscous and inertial forces, enabling minor perturbations to readily tip their balance.

From our evaluation of the multiplexing potential of the Venturi microregulator, we discovered the extreme sensitivity of microscale gas flows to geometric and surface nonuniformities. Because the variability that necessitated array tuning between individual microregulators in the same microregulator array did not change over time, geometric heterogeneity seemed the most likely culprit. In the context of flow control, this suggests that actively controlled geometric modulation may provide another viable means of flow perturbation. The problematic effect of unintentional surface irregularities in our fabricated geometries implies that small geometric changes—the mild deflection of a wall by a piezoelectric, for instance—can function as control mechanisms for gas flows.

Our modeling of the gas dynamics in planar micronozzles for *Re* between 10^2 and 10^3 supplied estimates of the magnitude and length scale of the viscous effects in these flows. We found that compressibility effects cause an increase in flow velocity with heat addition despite the simultaneous increase in viscous energy dissipation. The low dynamic viscosity of gases permits large velocity gradients in microchannel flows. In a choked microflow, it is easily possible for half the cross-section to be sonic while the region of the flow near the walls remains subsonic. This observation raises additional questions about microscale boundary layer-shock interactions and deviations from macroscale gas dynamics in the presence of such drastically nonuniform transverse velocity distributions.

Continuing Work

While designing the Venturi microregulator, the question arose of whether switching mechanisms other than thermal perturbation could perform comparably for microscale control of inertial gas flows. The concept of plasma generation for flow control in microchannels emerged from this discussion. The favorable scaling of electric field strength with decreasing length scale motivates the primary argument behind this idea. Due to the small characteristic lengths in microscale systems, nominal voltages can produce strong electric fields, facilitating the ionization of gas molecules and subsequent acceleration of the ionized particles.

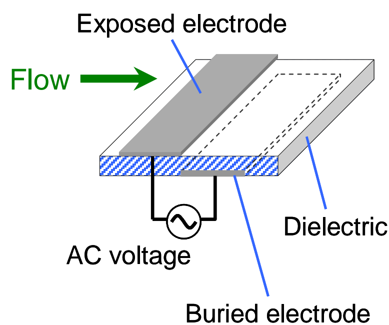

Figure 5.1. Schematic of a surface dielectric barrier discharge plasma actuator. Pairs of metal electrodes separated by a distance *d* are oriented such that their electric field is aligned with the direction of flow. One electrode is covered by a dielectric, and the other remains exposed to the gas to allow generation of a net force on the fluid above the surface when actuated by an appropriate AC voltage.

Numerous studies have demonstrated the capability of airflow control at atmospheric pressure using plasma actuators. The actuators consist of pairs of coplanar metal electrodes in which one electrode is exposed to the air and the other is covered by a dielectric as shown in Fig. 5.1. Upon application of an AC voltage of appropriate amplitude and frequency, a surface dielectric barrier discharge (DBD) is produced. This discharge exerts a net force, tangent to the surface, on the fluid directly above the actuator via collisions between the ionized particles and neutral gas molecules due to the asymmetry in ion density caused by the presence of the dielectric.[1] Most commonly, plasma actuators mounted on airfoils have been used to modify boundary layer behavior

in the presence of adverse pressure gradients. Images of such an experimental system by J.R. Roth are shown in Fig. 5.2.[2] Regulation of the direction and phase of the periodic momentum addition to the fluid can induce either boundary layer separation or reattachment at flow velocities up to 100 m s^{-1} and *Re* up to 500,000.[3] In still air, the same mechanism would enable bidirectional pumping tangent to the substrate.

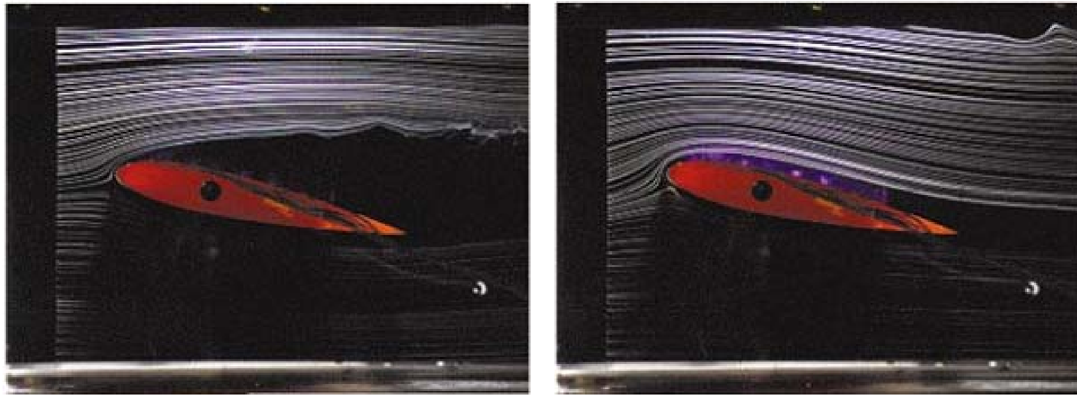

Figure 5.2. Plasma actuators mounted on an airfoil being used to control boundary layer separation. (*Left*) Boundary layer separation occurs due to the adverse pressure gradient formed on the trailing surface of the airfoil when the plasma is off. (*Right*) The momentum added by the plasma to the fluid near the airfoil surface causes the boundary layer to reattach. (Images taken from J.R. Roth, *Phys Plasmas* 2003.)

Continuous operation of plasma actuated flow control requires the generation of a stable DBD at atmospheric pressure. The desired DBD phenomenon occurs in the normal glow regime, identified in Fig. 5.3, where voltage requirements are at their minimum. The stability of the generated plasma depends strongly on the actuation frequency (v_0) and the electrode spacing (d). This dependence is best explained in the context of a conventional parallel plate plasma reactor in which the applied AC voltage forces the electrons and positive ions in the plasma volume to oscillate between the plate electrodes with each reversal of field polarity. The higher charge-to-mass ratio of the electrons causes them to travel farther than the heavier positive ions in the same electric field. A

stable glow discharge forms when the electrons can physically reach the electrodes to recombine or build up a surface charge while the ions remain trapped in the plasma volume. The frequency band in which this occurs is given by

$$\frac{eV_{rms}}{\pi m_i \nu_{ci} d^2} \leq \nu_0 \leq \frac{eV_{rms}}{\pi m_e \nu_{ce} d^2} \tag{5.1}$$

where e is the elementary charge; V_{rms} is the root mean square actuation voltage; m_{i} and m_{e} are the respective masses of the ions and electrons; and ν_{ci} and ν_{ce} are the respective collision frequencies of the ions (~ 10^{10} s^{-1}) and electrons (~ 10^{12} s^{-1}). If the actuation frequency falls below this range allowing both the ions and electrons to reach the electrodes during each half cycle, the plasma will not initiate. On the other hand, actuation frequencies falling above this range trap both the ions and electrons between the electrodes, resulting in a filamentary plasma rather than a uniform glow discharge.

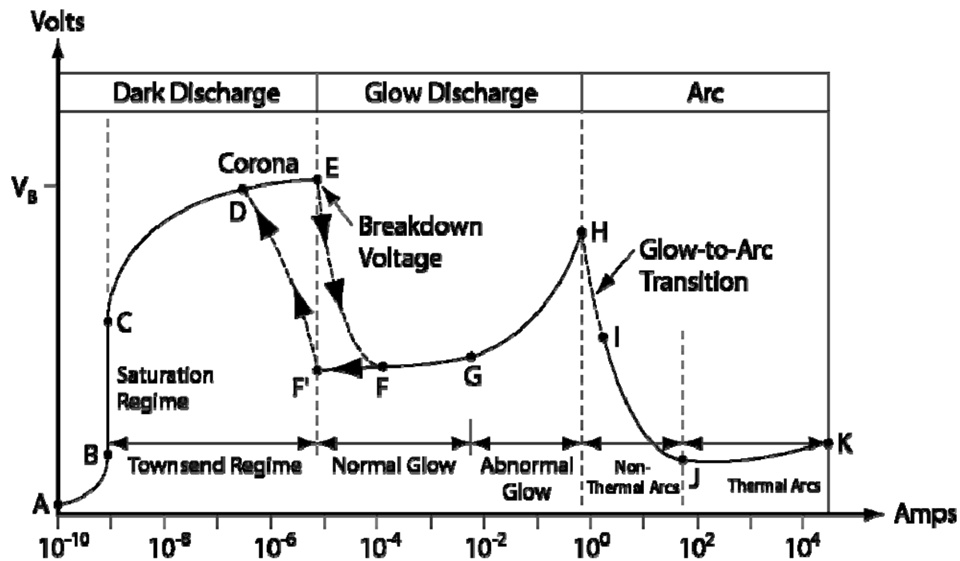

Figure 5.3. Voltage-current characteristics of low-density plasma discharge regimes. The lowest actuation voltage for a stable discharge occurs in the normal glow regime. (Graphic taken from J.R. Roth, Industrial Plasma Engineering: Volume I, 1995.)

The second major parameter in plasma actuator operation is the actuation voltage. Paschen's Law characterizes the breakdown voltage (V_b) of a gas between parallel plate electrodes as a function of pressure (P) and electrode spacing as follows:

$$V_b = \frac{a \cdot (Pd)}{\ln(Pd) + b} \tag{5.2}$$

where a and b are gas specific constants ($a = 43.6 \times 10^6$ V atm^{-1} m^{-1} and $b = 12.8$ for air). The form of Eqn. 5.2 indicates the existence of a minimum breakdown voltage at some critical value of Pd. The significance of this critical value is best explained in the context of the electron mean free path. At high pressures or large electrode spacings where mean free path is short relative to d, electrons encounter collision events with neutral gas species more frequently while traversing the electrode spacing over each half cycle. Because individual electrons lose energy with each collision, a higher voltage is needed for the electrons to accumulate sufficient energy to initiate an ionization avalanche. Conversely, at low pressures or small electrode spacings where the mean free path is long relative to d, the reduced frequency of collisions between electrons and neutrals necessitates higher voltages to produce sufficient ionization to ignite a plasma. Equation 5.2 predicts a minimum breakdown voltage of 327 V for an electrode spacing of 7.5 µm in air at a pressure of one atmosphere. However, this prediction has proven inaccurate with Paschen's Law deviating significantly from empirical observation for very small electrode spacings at high pressure (approximately $d < 10$ µm at one atmosphere). Based on Eqns. 5.1 and 5.2, $d = 200$ µm at a pressure of one atmosphere should correspond to a normal glow frequency band of 3.3 MHz to 1.7 GHz. Coplanar electrode configurations likely exhibit a slightly broader frequency band because of the curvature in the electric field lines, which should increase the effective electrode spacing.

The chief obstacle to successful implementation of a microscale plasma actuator is design of the powering circuit. Although the calculated actuation voltage is high, theoretical power consumption remains low (~ 3 W) due to the low current through the actuator. However, because the components required to produce the appropriate actuation voltages possess large reactive impedances, the efficiency of the powering circuit varies greatly with operating frequency. Impedance matching is thus imperative to limit the power draw to acceptable levels. We have fabricated multiple candidate electrode geometries, as shown in Fig. 5.4, to be tested pending implementation of the powering circuit. In continuing this work, several key questions regarding the viability of this technology for controlling microchannel flow merit further investigation: (1) Given that previous plasma actuator studies were all performed in unbounded flow systems, does the mechanism behave differently in a closely bounded flow? (2) How robust is the performance of the plasma actuator in the presence of significant back pressure, particularly resulting from surface tension if used to propel liquid volumes?

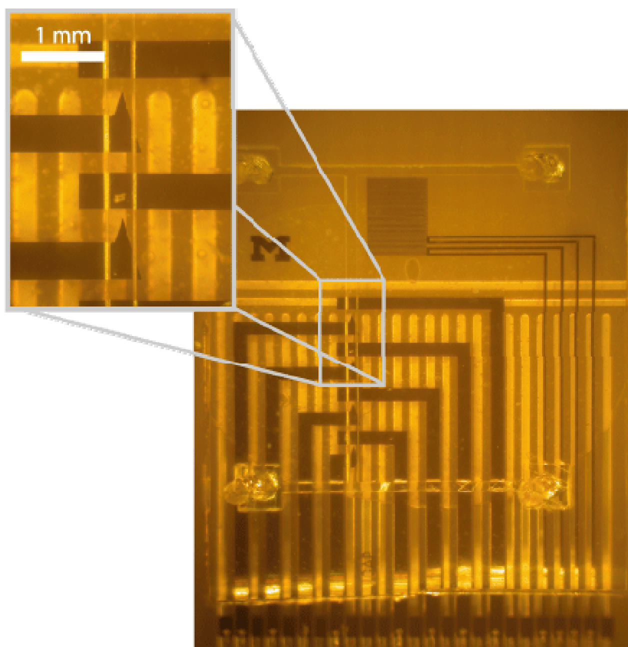

Figure 5.4. Candidate electrode geometry for microplasma actuator. The electrode pairs in this device are patterned in Ti/Au (300 Å/5000 Å) separated by a 3000 Å layer of Al_2O_3. The overlaid channel geometry was cast with PDMS.

References

[1] Font GI, Morgan WL (2005) Plasma discharges in atmospheric pressure oxygen for boundary layer separation control. AIAA Paper 2005−4632, 35th Fluid Dynamics Conference and Exhibit, Toronto, Ontario.

[2] Roth JR (2003) Aerodynamic flow acceleration using paraelectric and peristaltic electrohydrodynamic effects of a One Atmosphere Uniform Glow Discharge Plasma. Phys Plasmas 10:2117-2126.

[3] Moreau E (2007) Airflow control by non-thermal plasma actuators. J Phys D: Appl Phys 40:605-636. doi: 10.1088/0022-3727/40/3/S01

4 Roth JR (1995) Industrial plasma engineering: Volume I – Principles. Institute of Physics Press, Bristol. isbn: 0-7503-0318-2